Title: Cell type-specific basal forebrain GABAergic neuronal activity with olfactory task performance, learning, and decision-making

Authors: Elizabeth Hanson Moss[1], Evelyne K. Tantry[1], Elaine Le[1], Katie L. Brandel-Ankrapp[2], Benjamin R. Arenkiel[1*]

Affiliations: [1]Department of Molecular and Human Genetics, Baylor College of Medicine, Houston TX; [2]Neuroscience Graduate Program, Baylor College of Medicine, Houston, TX

*Corresponding author: arenkiel@bcm.edu

Abstract

Sensory perception relies on the flexible detection and interpretation of stimuli across variable contexts, conditions, and behavioral states. The basal forebrain is a hub for behavioral state regulation, supplying dense cholinergic and GABAergic projections to various brain regions involved in sensory processing. Of GABAergic neurons in the basal forebrain, parvalbumin (PV) and somatostatin (SST) subtypes serve opposing roles regulating behavioral states. To elucidate the role of basal forebrain circuits in sensory-guided behavior, we investigated GABAergic signaling dynamics during odor-guided decision-making. We used fiber photometry to record cell type-specific basal forebrain activity during an odor discrimination task and correlate temporal patterns of PV and SST neuronal activity with olfactory task performance. We found that PV-expressing GABAergic neurons are activated by odors and are selectively suppressed by reward. However, SST-expressing GABAergic neurons are activated during both odor and reward delivery. Notably, odor and reward responses of PV and SST neurons are uniquely correlated with behavioral measures of odor discrimination and decision bias. Additionally, as mice undergo discrimination learning, the magnitude of reward-related excitation decreases in SST neurons, while reward-related suppression increases in PV neurons. Finally, we show that chemogenetic inhibition of SST neurons alters decision bias to favor reward-seeking. These results suggest that subtypes of GABAergic basal forebrain neurons are differentially involved in decision-making, and that their bidirectional activity impacts decision making during olfactory guided behavior.

Introduction

Behavioral states such as mood, motivation, attention, and arousal potently influence neural circuit function and control information processing from the level of sensory perception to cognition, learning, and memory. The basal forebrain (BF) is heavily involved in behavioral state-dependent regulation, with BF circuits controlling directed attention (Sarter and Bruno, 1999; Sarter et al., 2001; Hasselmo and McGaughy, 2004; Herrero et al., 2008), sensory processing (Parikh et al., 2007; Chaudhury et al., 2009; Pinto et al., 2013; Bendahmane et al., 2016; Gritton et al., 2016; Ogg et al., 2018), feeding behavior (Herman et al., 2016; Patel et al., 2019), reward prediction and salience (Lau and Salzman, 2008; Lin and Nicolelis, 2008; Hangya et al., 2015; Ledbetter et al., 2016; Zhang et al., 2019), learning and memory (Muir et al., 1993; Devore et al., 2015; Harrison et al., 2016; Zheng et al., 2018), and arousal (Semba, 1991; Szymusiak, 1995; Sarter and Bruno, 1999; Szymusiak et al., 2000; Lau and Salzman, 2008; Anaclet et al., 2015; Xu et al., 2015). Notably, given that BF projections robustly target both sensory and cognitive circuits, their degeneration is thought to underlie cognitive deficits in disease (Bigl et al., 1982; Grothe et al., 2010; Ballinger et al., 2016; Chaves-Coira et al., 2016; Gielow and Zaborszky, 2017). During reward-based learning, BF responses to sensory stimuli are modulated by reward expectation (Lin and Nicolelis, 2008; Hangya et al., 2015; Zhang et al., 2019), supporting that BF circuits integrate sensory input with internal information about reward expectation. Additionally, blanket inhibition of the BF impairs the recruitment of attention in response to motivationally salient stimuli (Tashakori-Sabzevar and Ward, 2018). Intriguingly, both cholinergic and non-cholinergic neurons in the BF show distinct activation patterns in response to sensory stimuli and play different roles in reward-based learning (Hangya et al., 2015; Patel et al., 2019; Böhm et al., 2020; Nunez-Parra et al., 2020; Hanson et al., 2021). Thus, to understand how BF circuits mediate state-dependent effects on sensory perception and related behaviors, it is necessary to determine the dynamic activity patterns of specific cell types in the BF and how they are modulated across different behavioral contexts. To address this, we sought to determine cell type-specific BF responses to sensory input, how cell type-specific BF activity is modulated by reward-based learning, and how manipulating such activities affects decision making in a sensory discrimination task.

Cholinergic neurons in the BF regulate behavioral states such as attention and arousal, as well as information processing and synaptic plasticity at downstream targets (Markram and Segal, 1990; Hasselmo, 1999; Sarter and Bruno, 1999; Parikh et al., 2007; Goard and Dan, 2009; Zant et al., 2016). Notably, however, non-cholinergic neurons of the BF, including parvalbumin GABAergic (PV), somatostatin GABAergic (SST), and glutamatergic neurons, also play important roles regulating activity within the BF and at downstream targets throughout the brain (Gracia-Llanes et al., 2010; McDonald et al., 2011; Kim et al., 2015; Xu et al., 2015; Villar et al., 2020). For example, GABAergic projections from the BF to the cortex drive oscillations associated with consciousness and decision making (Kim et al., 2015), and such BF GABAergic control of population activity has been shown across a range cortical

and sensory projection targets (Zaborszky et al., 1986; Fisher et al., 1988; Sarter et al., 1999; Nunez-Parra et al., 2013; Agostinelli et al., 2019; Böhm et al., 2020; Villar et al., 2020). Importantly, however, different subtypes of BF GABAergic neurons play opposing roles in regulating behavioral states. For example, BF PV neurons have been shown to drive wakefulness, while SST neuronal activation promotes deep sleep (Xu et al., 2015) though see also (Anaclet et al., 2018). Additionally, BF PV and SST neurons exhibit opposite responses to acute changes in behavioral state, with PV neurons excited and SST neurons suppressed by a transition to running on a wheel (Harrison et al., 2016). Overall, the diverse cell types within the BF are highly interconnected (Zaborszky and Duque, 2000a; Xu et al., 2015), are functionally coordinated (Tingley et al., 2015), overlap substantially in their long-range projection targets (Zaborszky et al., 1986; Do et al., 2016; Böhm et al., 2020; Zheng et al., 2022), but play unique roles in behavioral state regulation (Xu et al., 2015; Harrison et al., 2016). As such, it has been challenging to address the question of how cell type-specific and state-dependent BF circuit activity influences sensory perception and behavior. Towards this we have set out to (1) resolve what information is represented in the neuronal activity of different BF cell types during complex behavioral tasks, and (2) determine how and when patterns of neuronal activity contribute to distinct aspects of a behavioral task that include stimulus detection, reward prediction, and decision making.

The olfactory system is an ideal model for examining the influence of BF modulation on sensory perception and decision-making behavior because both the olfactory bulb and the olfactory cortex receive significant cholinergic and GABAergic input from the BF (Woolf et al., 1986; Zaborszky et al., 1986; Nunez-Parra et al., 2013; Sanz Diez et al., 2019; Böhm et al., 2020). Also, convenient behavioral assays exist to determine olfactory discrimination abilities and odor-guided decision-making behavior. Studies examining the impact of BF neurons on odor processing have found that inhibiting BF GABAergic neurons impairs fine odor discrimination in a cross-habituation test (Nunez-Parra et al., 2013), and ablating BF cholinergic neurons impairs discrimination in a go/no-go task (Zheng et al., 2022). Moreover, both cholinergic and GABAergic BF neurons respond to odors and reinforcement in go/no-go discrimination tasks (Hangya et al., 2015; Nunez-Parra et al., 2020). We have previously shown that BF extracellular acetylcholine peaks during odor presentations and is suppressed by reward delivery in a go/no-go task. The changes in cholinergic tone mirror changes in BF GABAergic neuronal activity, demonstrating that BF GABAergic neurons are acutely and bidirectionally regulated during performance of the discrimination task (Hanson et al., 2021). These experiments, however, do not differentiate subtypes of GABAergic neurons and, thus, do not distinguish how patterns of PV or SST neuronal activity are uniquely correlated with behavior. Towards understanding how specific BF cell types respond to sensory stimulation, decision making, and discrimination learning, we used fiber photometry to differentially record the activities of BF PV and SST neurons while mice learned to discriminate odors in an olfactory-cued go/no-go discrimination task. Our results show distinct patterns of neuronal activity in PV and SST BF neurons which are uniquely correlated with discrete aspects of

task performance and decision making. Finally, chemogenetic inhibition of BF SST neurons indicates that they promote more optimal decision-making by lessening a bias toward reward-seeking behavior.

Results

BF PV neurons are excited by odor and suppressed by reward delivery

To assess PV neuronal responses during odor discrimination learning, we selectively expressed the genetically encoded calcium indicator GCamP8s in BF PV neurons by injecting an AAV expressing Cre-dependent GCaMP8s (AAV hsyn-FLEX-GCaMP8s) into the BF of PV-Cre mice. At the same time, we placed a fiberoptic implant over the horizontal limb of the diagonal band of Broca (HDB) in the BF (Figure 1A). Implant and viral targeting were verified via post hoc immunofluorescence imaging (Figure 1B, C). Implanted mice were then trained and tested on a go/no-go paradigm as previously described (Hanson et al., 2021). During training, mice learned to distinguish an S+ odorant associated with a water reward from an S- odorant not associated with reward. In this odor-cued go/no-go discrimination task, there were four trial outcomes depending on the odor presented and the decision to go or not go for a reward. Retrieving the water reward upon S+ cue presentation was considered a “Hit”. Not retrieving water after S+ presentation was considered a “Miss”. Attempting to retrieve water upon S- cue presentation was a “False Alarm”. Finally, initiating a new trial after S- presentation was considered a “Correct Reject” (Figure 1D). Punishment for False Alarm trials consisted of a 4 second time-out period in which they were unable to initiate another trial. Mice were trained on the go/no-go task for 10-14 days prior to testing and fiber photometry recording. After training, mice were tested on novel odor pairings (Table 1 in methods) while neuronal activity was recorded with fiber photometry. All mice effectively learned to discriminate new pairs of S+ and S- odors with performance significantly above chance within 400 trials (d’: 2.30 ± 0.17, $p < 0.0001$, Figure 1E). Variability in performance was likely due to randomization of S+ and S- odors across mice and sessions.

To determine HDB PV neuronal activity across phases of the go/no-go task and different trial outcomes, photometry traces were first aligned to odor port entry times and sorted by trial type. We observed a distinct pattern of PV neuronal activity over the course of a go/no-go trial with excitation during odor presentations across all trial types, and suppression following reward delivery in Hit trials (Figure 1F). The peak in z-scored PV neuronal activity during odor presentation was equivalent across all four trial types (Hit: 1.73 ± 0.21, Miss: 1.71 ± 0.20, Correct Reject: 1.64 ± 0.20, False Alarm: 1.68 ± 0.21 z score, $p = 0.40$) suggesting that the response was not odor specific (S+ vs. S-), predictive of behavioral choice (go vs. no-go), or predictive of accuracy (correct vs incorrect decisions) on individual trials (Figure 1G). To further examine the response of PV neurons to reward seeking and reinforcement, we realigned Hit and False Alarm trials to the timing of reward port entry (Figure 1H). Quantifying the area under the curve (AUC) for the first 5 seconds after reward port entry showed that PV neuronal activity was strongly suppressed in Hit, but not False Alarm trials (Hit: -2.52 ± 0.50, False Alarm: 2.60 ± 0.40 z score*s, $p < 0.001$), implying that the suppression was a consequence of obtaining the water reward (Figure 1I). Notably, this pattern of odor-evoked excitation and reward-evoked suppression mirrors the changes in both the cholinergic tone and general GABAergic neuronal activity

140 we have previously described in the HDB (Hanson et al., 2021). These data indicate that PV neurons in
141 the HDB respond bidirectionally to the odor cue and positive reinforcement during go/no-go task
142 performance, thus raising the question of whether PV neuronal activity controls or is modulated by task
143 performance across sessions and/or learning within sessions.

144

145 **BF PV neuronal activity changes with go/no-go task performance and learning**

146 To determine the extent to which PV neuronal activity was related to task performance, we examined
147 correlations between the odor response magnitude, reward response magnitude, behavioral
148 performance, and decision making. To quantify behavioral performance and decision making we used
149 the signal detection theory measures of d' and criterion (C). d' measures the sensitivity of odor
150 discrimination with higher d' values indicating more accurate discrimination between the S+ and S-
151 odors and chance equaling zero. Criterion measures the bias in decision-making toward reward
152 seeking (go) or non-reward-seeking (no-go) behavior with negative C values indicating a bias towards
153 reward-seeking behavior. Notably, in our go/no-go task, S+ and S- odors are presented with equal
154 frequency so that optimal decision bias in the task is 0. However, mice performed this task with a
155 significantly negative decision bias (i.e., a bias towards reward-seeking, C: -0.11 ± 0.05, $p < 0.05$ one
156 sample t test) likely because the positive possibility of a water reward outweighed the negative
157 possibility of a timeout punishment.

158 Using linear regression and Pearson's correlation to examine the relationship between PV
159 neuronal activity and sensitivity across sessions, we find that d' is negatively correlated with odor
160 response magnitude in Hit trials (Slope: -0.41 ± 0.17, R: -0.44, $p < 0.05$), Miss trials (Slope: $-0.42 \pm$
161 0.14, R: -0.52, $p < 0.01$), Correct Reject trials (Slope: -0.44 ± 0.17, R: -0.45, $p < 0.05$), and False Alarm
162 trials (Slope: -0.43 ± 0.17, R: -0.45, $p < 0.05$). These data show that in sessions where the average
163 odor response among HDB PV neurons was higher, overall performance on the discrimination task was
164 worse (Figure 2A). Using the same analysis to compare decision bias to PV neuronal activity, we found
165 that C was not correlated with the magnitude of the odor-evoked peak for any trial type (Figure 2B).
166 Together these data help distinguish between neuronal activity patterns related to decision making
167 behavior and task difficulty (i.e. the discriminability of individual odor pairs). While these data do not
168 indicate whether the magnitude of the PV odor response influences odor discrimination, they do
169 suggest that the odor-evoked peak in HDB PV neuronal activity is related to odor discriminability but not
170 decision-making behavior in this go/no-go task.

171 Next, we examined whether PV neuronal activity in response to reward delivery was related to
172 odor discriminability or decision-making behavior. Using the same linear regression and Pearson's
173 correlation analyses, we found no correlation between d' and the magnitude of the reward-evoked
174 suppression in Hit or False Alarm trials (Figure 2C). However, there was a significant difference in the

175 elevations of the regressions between Hit and False alarm trials (Hit: -1.68 ± 1.06, False Alarm: 2.90 ±
176 1.13, $p < 0.0001$) confirming that the difference in AUC between Hit and False Alarm trials is consistent
177 across sessions with a range of d'. At the same time, we found a significant negative correlation
178 between C and the magnitude of reward evoked suppression in Hit trials (Slope: -4.08 ± 1.10, R: -0.59,
179 $p < 0.01$). This correlation was absent in unrewarded False Alarm trials (Figure 2D). These data show
180 that the suppression of PV neuronal activity after reward delivery is related to decision making-
181 behavior, though they do not suggest whether the greater suppression drives more optimal decision-
182 making behavior or vice versa. Elevations were also significantly different between Hit and False Alarm
183 trials (Hit: -2.88 ± 1.10, False Alarm: 2.54 ± 1.44, $p < 0.0001$) confirming that the reward-evoked
184 suppression of PV neuronal activity is present across sessions with a range of decision biases.

185 Correlations between session averages of d' and criterion do not help determine whether odor
186 and reward-evoked suppression in PV neurons is modulated by changes in performance over the
187 course of a session (as performance changes with learning) or whether it is fixed within a session.
188 While these data demonstrate relationships between behavior and PV neuronal activity across
189 sessions, we also sought to determine whether and how PV activity patterns were modulated over the
190 course of odor learning. To examine this, we subdivided sessions into first blocks, including the first 20
191 trials of an odor pair, and best blocks, including the block of 20 trials with the highest accuracy in a
192 session. As expected, accuracy in the best blocks was consistently higher than accuracy in the first
193 blocks, demonstrating that the mice learned to discriminate the novel odor pairs over the course of the
194 sessions (Figure 2E). Interestingly, we found that the odor evoked peaks were not different between
195 first and best blocks (Figure 2F). However, the reward-evoked suppression of PV neuronal activity was
196 significantly greater in the best blocks compared to the first blocks (Change from first block to best
197 block: 1.81 ± 0.50, $p < 0.001$) (Figure 2 G, H). These data show that the reward-related suppression in
198 PV neurons changes with learning, and this suppression increases as mice improve at the
199 discrimination task. At the same time, the odor response in PV neurons does not change with learning.
200 This implies that PV odor responses are determined by the nature of the odor pairs, with harder pairs
201 evoking larger responses and easier pairs evoking smaller responses, even as a mouse's performance
202 changes over the course of a session.

203

204 **BF SST neurons are excited by both odor presentation and reward delivery**

205 Within the BF, PV neurons receive inhibitory input from neighboring SST neurons. This disinhibitory
206 circuit contributes to the opposing effects that BF SST and PV neurons have on arousal state (Xu et al.,
207 2015). Given the nature of this connectivity, we next asked whether inhibition from SST neurons may
208 contribute to the reward-evoked suppression that we observed in PV neurons. To evaluate how SST
209 neurons selectively respond during odor discrimination learning, we again used fiber photometry during

the go/no-go task. For this, we selectively expressed GCaMP in BF SST neurons and implanted a fiberoptic over the HDB (Figure 3A, B). As in PV-Cre mice, the overall performance of SST-Cre mice on new odor pairs was variable (d': 1.24 $\pm$ 0.3) due to the randomization of odor pairs across mice and sessions (Figure 3C, D). Aligning the photometry traces to odor port entry times revealed that SST neurons were excited by odor presentation (Figure 3E) and that this excitation was equivalent across trial types (Hit: 1.06 $\pm$ 0.24, Miss: 1.10 $\pm$ 0.29, Correct Reject: 1.01 $\pm$ 0.20, False Alarm: 0.94 $\pm$ 0.23, $p = 0.30$) (Figure 3F). This response was similar to the excitation that we observed in PV neurons upon odor presentation. Notably, however, when traces were aligned to reward port entry (Figure 3G) we found that SST neurons were also activated by reward delivery (Hit AUC: 0.21 $\pm$ 0.13, False Alarm AUC: -0.132 $\pm$ 0.14, $p < 0.01$), in contrast to the suppression we observed in PV neurons (Figure 3H). These data suggest that SST and PV neurons in the HDB exhibit opposing responses to reward delivery. While these data do not show that SST excitation drives the reward related suppression in PV neurons, they support the hypothesis that SST and PV neurons are playing opposing roles in go/no-go task reinforcement. This raises the question of how SST neuronal activity is correlated with behavioral performance and decision-making, and to what extent the correlations oppose those observed in PV neurons.

BF SST neuronal activity changes with go/no-go task performance and learning

With the goal of directly comparing the two primary GABAergic neuronal subtypes in the HDB, we conducted the same analysis of SST neuronal activity as we did previously for PV neurons across the range of go/no-go task performance. To determine the extent to which SST neuronal activity related to task performance, we examined correlations between the SST odor response magnitude, reward response magnitude, behavioral performance, and decision making. In contrast to PV neurons, we found no correlation between d' and SST odor response magnitude, nor did we observe differences between trial types in the relationship between odor response magnitude and d' (Figure 4A). However, for trials in which the S+ odor was presented, we found a significant positive correlation between odor response magnitude and response bias (Figure 4B). This implies that in Hit trials (Slope: R: 0.23, $p < 0.05$) and Miss trials (Slope: R: 0.26 $p < 0.05$), the larger S+ odor-evoked response in SST neurons was correlated with a more optimal decision bias (i.e. closer to zero). Without a substantial number of sessions with decision bias above zero, however, we cannot determine whether the relationship would continue increasing linearly as criterion values become suboptimal in the positive direction. Therefore, it remains a question whether larger S+ odor responses in SST neurons are related to optimal decision-making behavior, or whether larger odor responses reflect decision biases away from reward seeking behavior.

While we did not find a relationship between SST odor responses and d', when traces were aligned to reward port entry, we found a significant negative correlation between the magnitude of the reward-related response (AUC) and d' across sessions (Figure 4C). This negative correlation was only significant in Hit trials (Slope: -0.20, R: -0.37, $p < 0.05$), whereas False Alarm trials showed no correlation. Additionally, comparing the intercepts of the best fit lines between Hit and False Alarm trials, we found no significant difference ($p = 0.18$). Taken together with our finding that overall reward-related excitation of SST neurons is larger in Hit trials than in False Alarms (Figure 3H), this linear regression analysis indicates that the difference between Hits and False Alarms is greatest in sessions with lower overall d' values (indicating worse task performance), and it is not consistent in sessions with better performance. Comparing reward response magnitudes to decision bias, we found no correlation between criterion and reward response for Hits or False Alarms (Figure 4D). However, we did observe a significant difference between the elevations of the regressions for Hits vs. False Alarms ($p < 0.05$), confirming that increased reward responses in Hit trials compared to False Alarms remained consistent across a range of decision biases.

Importantly, correlating neuronal activity with session averages of d' and criterion do not help determine whether odor and reward-evoked responses in SST neurons are modulated by moment-to-moment changes in performance within sessions (i.e. as performance changes with learning), or whether neuronal activity patterns are fixed within a session. For example, it is possible that the negative correlation between reward response magnitude and discrimination sensitivity (Figure 4C) reflects overall lower excitation of SST neurons when rewards are obtained in sessions with easier odor pairs (and, therefore, higher overall d'). In this case the magnitude of the reward response would be a feature of the odor pair and would remain fixed within a session even as performance changed with learning. Thus, to determine how patterns of SST neuronal activity are modulated by changes in task performance with learning, we next examined how odor and reward responses changed within go/no-go sessions, as mice improved at the discrimination task. To examine performance-related changes, we subdivided sessions into first blocks and best blocks (as described for PV neuronal recordings), with first blocks showing significantly lower accuracy (Figure 4E). Aligning first and best block Hit trials to trial initiation revealed no differences in odor-evoked peaks in SST neuronal activity (Figure 4F), suggesting that SST odor responses are determined by the identity of the odor pair, and are not modulated by learning. However, aligning Hit trials to reward port entry revealed a significant reduction in reward-related excitation of SST neurons in the best blocks (Best Block AUC: -1.50 ± 0.48) compared to the first blocks (First Block AUC: 1.305 ± 0.63, $p < 0.001$) (Figure 4G, H). Taken together with the negative correlation between session average d' values and reward-related excitation (Figure 4C), these data suggest that reward responses of SST neurons are modulated by performance, with improvements in discrimination leading to a reduction in reward related excitation both across odor pairs with a range of difficulties, and within sessions, as mice learn to discriminate new S+ and S- odor pairs.

281

282 **DREADD-mediated inhibition of SST neurons does not impact firing of neighboring BF neurons**

283 We next sought to determine how directly manipulating BF GABAergic signaling impacted odor
284 discrimination and decision-making behavior. Towards this, we selectively expressed the inhibitory
285 DREADD hM4Di in BF SST neurons (Figure 5A-C). Treatment with the DREADD ligand CNO showed
286 targeted and ligand-dependent inhibition in Hm4Di-expressing SST neurons. We chose SST neurons
287 for manipulation because they have been shown previously to make local inhibitory synapses onto
288 each of the other major cell types within the HDB, including PV GABAergic, glutamatergic, and
289 cholinergic neurons (Zaborszky and Duque, 2000a; Xu et al., 2015). To determine the direct effect of
290 CNO treatment on hM4Di expressing SST neurons, we made acute brain slices harboring the HDB for
291 whole cell electrophysiological recordings. After current clamping mCherry labeled, hM4Di-expressing
292 neurons (Figure 5D) we made stepped current injections from -100 to 180 pA before and after CNO
293 application (10 μM). Prior to CNO, SST neurons showed fast-spiking patterns with narrow action
294 potentials as previously described (Anaclet et al., 2018) (Figure 5E). As expected, we found that CNO
295 significantly inhibited action potential firing in hM4Di expressing HDB SST neurons at current steps of
296 60 pA or greater (Figure 5F), though we did not observe systematic hyperpolarization with CNO (ΔVm -
297 2.18 $\pm$ 1.95, $p = 0.33$) (Figure 5F, inset). To examine whether inhibition of SST neurons impacted firing
298 properties of neighboring HDB neurons, we also patched and current clamped unlabeled, non-hM4Di-
299 expressing neurons (Figure 5G). Unlabeled neurons were slow spiking and susceptible to
300 depolarization block, suggesting that they represented cholinergic or glutamatergic subtypes (Figure
301 5H). We found that CNO treatment neither reduced, nor enhanced the firing of the non-hM4Di
302 expressing neurons in the HDB (Figure 5I). CNO application did, however, cause depolarization in non-
303 hM4Di-expressing neurons (ΔVm 3.22 $\pm$ 0.73, $p < 0.01$) (Figure 5I, inset). Notably, current injection data
304 demonstrated that the observed depolarization did not alter the overall firing properties of non-hM4Di-
305 expressing neurons. While these data indicate that reducing the ability of SST neurons to fire action
306 potentials does not significantly impact the ability of the other HDB neurons to fire action potentials
307 when driven, they do not show how DREADD-mediated inhibition of SST neurons impacts HDB circuit
308 activity *in vivo* or during behavior.

309

310 **DREADD inhibition of SST neurons increases decision bias in go/no-go task**

311 To directly examine the role of BF SST neurons in odor discrimination and decision-making behavior,
312 we next selectively targeted hM4Di expression to BF SST neurons in HDB, the magnocellular preoptic
313 nucleus (MCPO), and substantia innominata (SI) – regions forming a complex within the BF that is
314 densely interconnected with olfactory brain regions (Zheng et al., 2018) (Figure 6A). We then trained
315 mice on the go/no-go odor discrimination task and tested how they performed in sessions with or

without CNO treatment. In a subset of mice, mCherry lacking hM4Di was selectively expressed in SST neurons to serve as controls for CNO treatment. After training, mice were tested on new S+/S- odor pairs for consecutive days until they either (1) successfully learned the new odor associations (achieved two consecutive blocks of 85% accuracy) or (2) failed to meet the criteria for learning three days in a row (Figure 6B). Odor pairs were then chosen to span a range of difficulties and were approximately matched in difficulty between CNO and Vehicle treated sets of odors (Table 2 in methods). Mice were treated with either CNO (3.5 mg/kg) or Vehicle (1% DMSO in saline) for each day of alternating odor pairs (Figure 6B). Sessions across multiple days of the same odor pair received the same CNO or Vehicle treatment and were concatenated into single sessions from which sensitivity and decision bias measures (d' and C) were calculated. Despite our earlier finding that discrimination sensitivity was inversely correlated with reward related excitation in SST neurons, we found that inhibiting SST neurons did not impact odor discrimination at the level of whole sessions (Figure 6C). Additionally, inhibiting SST neurons did not impact the rate at which mice learned new odor associations (Figure 6D). These data suggest that odor and reward evoked excitation of HDB SST neurons does not directly impact odor discrimination or odor discrimination learning. Notably, however, we found that decision bias was significantly altered by CNO treatment in hM4Di expressing mice (Figure 6E). When HDB SST neurons were inhibited, mice showed a significantly stronger bias toward reward seeking behavior (i.e. a more negative C value). Moreover, this bias towards reward seeking moved decision making further away from the optimal decision bias of zero for the go/no-go task. Together, these data suggest that HDB SST neurons play a distinct role in decision making behavior, without directly impacting discrimination ability or learning in this version of a freely moving, self-initiated, go/no-go discrimination task.

Discussion

The BF is a central hub for the regulation of behavioral states. Particular attention has been paid to the role of BF cholinergic neurons, which mediate effects of attention and arousal at downstream circuits, and which are disproportionately affected by neurodegenerative diseases like Alzheimer's and Parkinson's (Sarter and Bruno, 1997; Levin and Simon, 1998; Sarter et al., 2001; Grothe et al., 2010; Parrao et al., 2012). Cholinergic neurons respond directly to sensory cues, positive and negative reinforcement during learning, and changes in behavioral states across multiple timescales (Phillis, 1968; Szymusiak, 1995; Sarter and Bruno, 1999; Hasselmo and McGaughy, 2004; Parikh et al., 2007; Chaudhury et al., 2009; Hangya et al., 2015; Xu et al., 2015; Ruivo et al., 2017; Patel et al., 2019). Activity of non-cholinergic neurons in the BF is also correlated with behavioral state, sensory perception, and performance on behavioral tasks (Hassani et al., 2009; Devore et al., 2015; Hangya et al., 2015; Xu et al., 2015; Harrison et al., 2016). Previous studies using auditory, visual, and olfactory cues have found increased activity in BF neurons in response to conditioned stimuli, positive and

negative reinforcement, and in anticipation of salient stimuli (Lin and Nicolelis, 2008; Hangya et al., 2015; Zheng et al., 2018; Nunez-Parra et al., 2020). Specifically, BF neuronal activity is modulated by expectation, with more surprising reinforcement eliciting larger increases in firing for both cholinergic (Hangya et al., 2015) and non-cholinergic BF neurons (Lin and Nicolelis, 2008; Zheng et al., 2018). However, discrepancies exist across sensory systems regarding whether unconditioned stimuli evoke BF activity, and what proportion of BF neurons are excited versus suppressed by stimuli and reinforcement. For example, in auditory cued tasks, BF neurons only respond to conditioned stimuli (Lin and Nicolelis, 2008) whereas, in olfactory tasks, both cholinergic and non-cholinergic BF neurons respond to conditioned stimuli, unconditioned stimuli, and both positive and negative reinforcement – though modulation by expectation and learning is inconsistent across studies (Hangya et al., 2015; Nunez-Parra et al., 2020; Hanson et al., 2021). Additionally, a significant proportion of BF neurons show suppression in response to odor stimuli and positive reinforcement (Nunez-Parra et al., 2020), with GABAergic neurons showing suppression after positive reinforcement (Hanson et al., 2021). Notably, these previous studies have either separated cholinergic from non-cholinergic neurons using optogenetic tagging, or they recorded activity from the entire population of GABAergic neurons in the basal forebrain. As such, they were unable to differentiate between subtypes of non-cholinergic neurons, including PV-expressing and SST-expressing GABAergic neurons. Here, we selectively and independently target these two primary subtypes of GABAergic neurons, with the goal of determining how they uniquely contribute to BF population activity during olfactory discrimination learning.

In the olfactory system, the BF sends extensive cholinergic and GABAergic projections to the olfactory bulb (OB) (Zaborszky et al., 1986). Cholinergic projections target a subset of OB interneurons and mitral cells where they impact fine discrimination, short term odor memory, mitral cell tuning, synchronization, and excitability (Elaagouby et al., 1991; Castillo et al., 1999; Mandairon et al., 2006; Tsuno et al., 2008; Ma and Luo, 2012; Rothermel and Wachowiak, 2014; Rothermel et al., 2014; Bendahmane et al., 2016; Ogg et al., 2018; Böhm et al., 2020). GABAergic projections, on the other hand, preferentially target specific GABAergic interneurons in the OB, where they influence the survival of adult born neurons, fine odor discrimination, and signal to noise ratio (Böhm et al., 2020; Hanson et al., 2020; de Saint Jan, 2022). Additionally, a direct comparison of the impact of BF cholinergic and GABAergic projections on OB activity reveals that BF GABAergic neurons preferentially increase odor-evoked mitral cell firing and suppress spontaneous activity, while cholinergic neurons increase spontaneous, sniff-locked, and odor evoked mitral cell firing (Böhm et al., 2020). Thus, it has been well-established that BF cholinergic and GABAergic projections to the olfactory system impact olfactory sensory processing, particularly during learning and fine discrimination. At the same time, BF GABAergic neurons synapse extensively within the BF onto glutamatergic, cholinergic, and other GABAergic neurons, endowing the GABAergic neurons with a large amount of control over BF circuit activity as a whole (Zaborszky and Duque, 2000b; Xu et al., 2015). Within the population of GABAergic neurons that reside in the BF, however, the two major subtypes, Parvalbumin-expressing (PV) and

389 Somatostatin-expressing (SST) are correlated with and control behavioral states in opposing ways (Xu
390 et al., 2015; Harrison et al., 2016) making it difficult to draw conclusions about the independent roles of
391 these BF GABAergic neuron subtypes in sensory perception, attention, decision-making, and behavior.

392 Here, we separately targeted PV and SST neurons in the BF and recorded their activity during
393 olfactory guided behavior. We show that, while both neuronal subtypes are excited by odor stimuli,
394 each subtype responds in opposite ways to positive reinforcement. More specifically, SST neurons are
395 briefly excited by reward delivery, while PV neurons show a sustained suppression after obtaining a
396 reward. The opposite responses of PV and SST neurons to reinforcement mirrors the opposing roles of
397 PV and SST neurons in behavioral state regulation. While opposing responses in PV and SST
398 populations may be driven, in part, by direct inhibition of PV neurons by SST neurons in the BF, the
399 congruency of their responses to odor stimuli suggest that this relationship is more complicated. It is
400 possible, for example, that the inhibitory input from SST to PV neurons is gated differently in response
401 to external sensory inputs, than for internal state and/or reinforcement information. While our findings
402 do not suggest specific gating mechanisms, they do reveal a clear divergence in how BF circuits
403 encode sensory inputs and reinforcement feedback.

404 To further disambiguate responses to external sensory input from responses driven by internal,
405 reinforcement and learning related information, we extracted odor and reward evoked responses by
406 trial type from individual behavioral sessions and correlated their magnitude with behavioral measures
407 of odor discrimination sensitivity (d') and decision bias (criterion, C) (Stanislaw and Todorov, 1999).
408 Applied to our olfactory cued go/no-go discrimination task, d' reflects externally driven sensory
409 processing, and C reflects internally driven decision-making behavior. To address the question of
410 whether PV or SST odor responses are related to odor discrimination ability we examined correlations
411 between d' and odor response magnitudes across go/no-go sessions. When recording activity in PV
412 neurons, we found a negative correlation between odor response magnitude and discrimination
413 sensitivity. These data suggest that in sessions with overall worse performance (when odor pairs were
414 inherently harder to discriminate and/or when mice learned more slowly) PV neurons responded to both
415 S+ and S- odors more strongly. Importantly, however, PV odor responses did not systematically
416 change within sessions as mice improved at discriminating a given odor pair. This is supported by the
417 similar odor response magnitude observed in PV neurons from the early to later sessions after an odor
418 pair is learned. Together these data suggest that PV odor responses are influenced by the inherent
419 difficulty of an odor pair in the discrimination task such that, even as mice learn and improve at
420 discrimination over the course of a session, odor responses of BF PV neurons remained fixed. As such,
421 a role for BF PV neurons may be to preferentially signal to downstream circuits and coordinate
422 downstream population activity when the olfactory discrimination task is more difficult. In contrast to the
423 PV odor responses, the response of SST neurons to odors was not correlated with discrimination
424 sensitivity. However, the SST response to S+ odors (in Hit and Miss trials) was weakly correlated with

425 decision bias. That is, more negative criterion scores indicated a bias toward reward seeking behavior,
426 while criterion scores close to zero reflected optimal decision bias in our go/no-go task. Therefore,
427 these data suggest that in sessions with more optimal decision bias, SST neurons respond more
428 strongly to S+ odors. Notably, these data agree with, and are supported by, our finding that
429 chemogenetic inhibition of BF SST neurons drives less optimal decision- making behavior, biased more
430 strongly toward reward-seeking. Collectively, these data suggest that the strength of the odor response
431 in BF SST neurons may help determine subsequent decisions about whether to seek a reward when
432 stimulus identities are uncertain.

433 The opposing responses of PV and SST neurons to reward delivery are intriguing because they
434 mirror the opposite responses of BF GABAergic neurons to changes in behavioral state (Xu et al.,
435 2015; Harrison et al., 2016). This suggests that the two cell types play distinct roles in the response to
436 positive reinforcement during discrimination learning, though whether each cell type's activity impacts
437 discrimination or alters decision making is not clear. Correlating the magnitude of each cell type's
438 reward-related responses to discrimination sensitivity and decision bias provides insight into their
439 potential roles, if not information about causal mechanisms. Along these lines, we found that the
440 prolonged, reward-related suppression of PV neurons is inversely correlated with decision bias, such
441 that larger suppression occurs in sessions with more optimal decision bias. However, we see no
442 correlation of PV reward-related suppression with discrimination sensitivity. Notably, more optimal
443 decision bias within a session does not necessarily translate into better performance for that session –
444 in sessions with more optimal decision bias, mice still make errors, but the types of errors are balanced
445 between false alarms and misses. In sessions where mice are biased toward reward-seeking (false
446 alarm) errors, the reward related suppression of PV neurons is less pronounced. While it is possible
447 that the reward related suppression of PV neurons leads to more optimal decision-making behavior, it is
448 also possible, if not more likely, that under circumstances where mice preform a task with more optimal
449 decision bias, the upstream behavioral state and context dependent factors that control decision bias
450 also drive a larger reward-related suppression of BF PV neurons. SST neurons, on the other hand, are
451 briefly excited by reward delivery, and while the magnitude of their reward response is not related to
452 decision bias, it is inversely correlated with discrimination sensitivity. Such inverse correlation indicates
453 that the reward response in SST neurons is larger in sessions with poor performance, and smaller in
454 sessions with better overall performance, possibly indicating that SST excitation is modulated by
455 reward expectation. Notably, the correlation between d' and SST reward responses was also present
456 within sessions, implying that as mice learned to discriminate a given odor pair, reward-evoked
457 responses in SST neurons diminish.

458 Importantly, we also have to consider that the correlations observed between neuronal activity
459 and behavioral performance could be due to neuronal activity causing behavioral changes, behavioral
460 changes causing changes in BF neuronal activity, or a larger contextual or state change that may

impact neuronal activity and changes in behavior. SST neurons are intriguing components of the BF circuit because they directly inhibit each of the other major cell types in the BF, including glutamatergic, cholinergic, and PV GABAergic neurons. Notably, these previously described patterns of synaptic connectivity in the BF were revealed with optogenetic circuit mapping. In all its utility, it must also be considered that optogenetic circuit mapping leverages artificial, channel rhodopsin-mediated stimulation of SST neurons and, thus, does not indicate the extent to which SST synapses affect the activity of downstream BF neurons during normal circuit activity. To help better determine the impact of SST neuronal excitability on other cell types of the BF, we expressed an inhibitory DREADD in SST neurons and then measured action potential firing and resting membrane potentials in DREADD and non-DREADD expressing neurons. While CNO treatment effectively inhibited action potential firing of SST neurons driven by current injections, it did not systematically alter action potential firing in neighboring non-DREADD expressing neurons. However, CNO treatment did lead to a slight increase in the resting membrane potential of non-DREADD expressing neurons. This suggests that SST neurons may be tonically inhibiting neighboring BF neurons, and that DREADD-mediated inhibition of SST neurons relieves some of this inhibition, raising the resting potential of neighboring neurons.

To investigate whether SST neuronal activity was driving behavioral changes, as suggested by the correlation analysis, we inhibited SST neurons during a subset of go/no-go testing sessions. Based on our observed correlations, we predicted that (1) if SST excitation was driving more optimal decision-making behavior, then inhibiting SST neurons would lead to more negative decision biases, (2) if the reward-related excitation of SST neurons was causing poor discrimination, then inhibiting SST neurons would improve sensitivity, and (3) if a reduction in SST reward-related excitation facilitated learning, then inhibiting SST neurons would increase the rate at which d' improved within sessions. Indeed, DREADD-mediated inhibition of SST neurons lead to a reduction in criterion scores with no change in discrimination within or across sessions, indicating that SST neuronal activity influences decision-making behavior without altering discrimination. Together, our data highlight the unique activity of BF GABAergic PV and SST neurons in response to sensory and reinforcement information. Collectively, our results paint a nuanced picture of how odor and reward information are processed in the basal forebrain by the separate cell types and, importantly, they reveal how BF GABAergic neurons are uniquely involved in odor-guided decision-making behavior.

490 **Methods**

491 **Mice**

492 Mice were maintained on a 12-h light-dark cycle and were treated in compliance with the ethical
493 guidelines of the US Department of Health and Human Services and approved by IACUC at Baylor
494 College of Medicine. Both male and female mice over 2 months of age were included for all
495 experiments. SST-Cre (JAX#: 13044) and PV-Cre (JAX#: 17320) mice were originally purchased from
496 Jackson Laboratories.

497

498 **Surgery and viral constructs**

499 Surgical procedures were performed under general anesthesia using isoflurane (4% v/v) induction and
500 maintained under isoflurane with O2 (1-2% v/v) inhalation. Following anesthetic induction, mice were
501 secured to a stereotaxic frame and administered 5 mg/kg of meloxicam prior to surgery. All procedures
502 were carried out using to Angle 2 software (Leica Biosystems) to set and locate coordinates.
503 Craniotomies were performed over the horizontal diagonal band of Broca (HDB) at the coordinates from
504 Bregma: ML +/- 1 mm; AP 0.7 mm; DV -5.4 mm. To target the HDB for viral expression of calcium-
505 indicator GCaMP6f, cohorts of PV-Cre (N = 6) and SST-Cre (N = 8) mice were unilaterally injected with
506 250 nL of hSyn-Flex-GCaMP8s-WPRE. Following viral injection, a custom fiber optic implant (0.48 na,
507 200 um core diameter, RWD systems) was placed so that the tip of the fiberoptic was 0.1 mm dorsal to
508 the HDB coordinates used for viral injection. The implant was then fixed with Metabond dental cement
509 (Parkell). For inhibitory DREADD expression, SST-Cre mice were bilaterally injected with 250 nL of AAV-
510 DIO-hM4Di-mCherry (N = 8) or AAV-DIO-mCherry (N = 6) at the same HDB coordinates. Viral expression
511 reliably spread throughout the HDB, MCPO, and SI – regions that form a complex densely interconnected
512 with olfactory brain regions (Zheng et al., 2018). All mice were given a 2-week recovery period prior to
513 the start of behavioral testing. HDB/MCPO/SI targeting was verified in all cases with post hoc
514 immunofluorescence imaging of viral expression within the HDB.

515

516 **Go/no-go training**

517 Freely moving mice were trained on an olfactory-cued go/no-go discrimination task using olfactory
518 conditioning boxes (Med Associates) controlled by MedPC software. Conditioning boxes included one
519 odor delivery port and one water reward port, both equipped with IR beams to record port entries. The
520 odor delivery port received a constant stream of clean room air, cleared by a vacuum. Odors (Tables 1
521 and 2, Sigma) were injected into the steady air stream by opening valves to one of two odor reservoirs,
522 allowing the air stream to pass through the head space of the reservoir carrying the volatized odorant.
523 Reservoirs were 20 mL in volume and included 2.5 mL of odorant diluted to 1% by volume in mineral oil.

524 Water rewards were dispensed at 5uL in volume in the separate reward port upon reward port entry only
525 on correctly decided Hit trials. Conditioning boxes were housed within larger behavior isolation boxes
526 (Med Associates). Box fans in the isolation boxes continuously circulated ambient air away from the
527 conditioning boxes and out of the isolation boxes to reduce the accumulation of ambient odor.

528 Over the course of 10-14 days, mice underwent 5 stages of behavior-shaping as previously
529 described (Hanson et al., 2021). Mice were water restricted to no less than 85% of their body weight
530 during the 48 hours prior to the start of training. Mice were first trained to seek water rewards, then to
531 initiate trials by poking their nose into the odor port. Mice were then trained to respond to an S+ odor cue
532 (1% Eugenol in mineral oil) to receive a water reward. Upon forming this association, the S- odor cue
533 (1% Methylsalicylate in mineral oil) was introduced, in which mice were trained to refrain from seeking a
534 reward and instead initiate another trial. Trials required mice to sample the odor cues for 100ms or more
535 before responding to the cue and were categorized based on the S+/- odor cue and the mouse's
536 response. When mice were presented with the S+ odor cue, trials were considered "Hits" when mice
537 sought a water reward within 5s and "Misses" if mice did not enter the reward port. Trials in which the S-
538 odor cue was delivered were considered "False Alarms" when mice incorrectly attempted to retrieve water
539 and "Correct Rejects" if mice did not seek water. False alarms resulted in a 4-second time out
540 punishment. Accuracy was calculated as percent correct trials (hit + correct reject trials) for blocks of 20
541 trials. For each training session, mice completed 10-20 blocks. Training was considered complete after
542 mice completed a session with the training odors (Eugenol = S+, Methysalicylate = S-) in which they
543 achieved higher than 85% accuracy in at least 2 consecutive blocks. Testing sessions followed the same
544 pattern as the last stage of training, but new odor pairs were introduced, requiring mice to learn new S+
545 and S- odor associations (Tables 1 and 2).

546

547 **Go/no-go testing with fiber photometry**

548 For go/no-go testing with concurrent photometry mice were attached to a fiberoptic cable, connected to
549 a two-channel fiber photometry recording system (Doric) via a rotary joint in the top of the behavior box.
550 Odor pairs for photometry experiments were chosen randomly for each mouse and session from the list
551 in Table 1 so that each odor was never presented on more than one day. The timing of trial initiations
552 and reward port entries were measured by IR beams in the odor and reward ports. Port entry timings,
553 odor presentations, and trial outcomes were recorded with (Med Associates). The timing of each odor
554 presentation was output to the photometry recording system as a TTL pulse lasting the duration of an
555 odor presentation allowing synchronization of the photometry and behavior. Sessions were excluded if
556 mice failed to complete at least 100 trials and if the average d' value across the whole session was less
557 than 0.25.

558

559 **Table 1: Odors used in go/no-go experiments with fiber photometry**

Odor	*Molecular Weight (g/mol)*	*Vapor Pressure (mmHg)*	*Functional Group*	*Cat. Number*
Isovaleric Acid	102.13	0.44	Carboxylic acid 5C	31024
(+) Carvone	150.22	0.16	Cyclic ketone 10C 1 double bond	124931
(-) Carvone	150.22	0.16	Cyclic ketone 10C 1 double bond	22070
1-Methylpyrrole	81.12	15.00	Cyclic nitrogen	509973
Acetophenone	120.15	0.40	Aromatic ketone	200905
Guaiacol	124.14	0.10	Aromatic ether, alcohol	253200
P-Toyl Acetate	150.17	0.16	Aromatic ester, 7C	307300
Amyl Acetate	130.00	4.00	Ester 7C	504009
1-Octen-3-ol	128.22	0.53	Alcohol, 8C	280518
(+) Limonene	136.23	2.00	Cyclic 10C 2 double bond	183164
(-) Limonene	136.23	2.00	Cyclic 10C 2 double bond	218367
Benzaldehyde	106.12	1.00	Aromatic aldehyde	B1334
Isoamyl Acetate	130.19	4.00	Ester 7C	205508
1,4-Cineole	154.25	1.93	Cyclic oxygen, ether	27393
2-Methypyrazine	94.12	9.69	Pyrazine	75608
2-Ethylphenol	122.16	0.15	Aromatic alcohol	44000
Citral	152.24	0.22	Aldehyde	83007
2,6 Dimethyl-5-heptenal	140.22	0.62	Aldehyde, 8C	238902
alpha-Pinene	136.24	3.00	Cyclic 7C 1 double bond	147524
Cyclohexanol	100.16	0.66	Cyclic alcohol	105899
Allyl Sulfide	114.00	9.22	Sulfide	A35801
1-Butenol	74.12	7.00	Alcohol, 4C	281549
1-Pentanol	88.15	44.6	Alcohol, 5C	138975
2-Heptanol	116.20	1.00	Alcohol, 7C	328804
1-Hexanol	102.18	1.00	Alcohol 6C	H13303
1-Heptanol	116.20	0.22	Alcohol 7C	H2805
1-Octanol	130.23	0.14	Alcohol 8C	297887
Butylbenzene	134.22	1.03	Aromatic 10C	686859
Cyclobutanecarboxylic Acid	100.12	0.18	Cyclic carboxylic acid 5C	C95609
P-Cymene	134.21	1.50	Aromatic 10C	30039
Decane	142.29	1.43	Hydrocarbon	30540
Diethylbenzene	134.22	1.03	Aromatic 10C	D91055
2,3-Hexanendione	114.14	10.00	Ketone, 6C	255801
alpha-Phellandrene	136.24	1.86	Cyclic 10C 2 double bond	285609
Isoamyl Butyrate	158.00	0.95	Ester 9C	206008
Menthone	154.00	0.50	Cyclic ketone 10C	218235
2-Heptanone	114.18	3.00	Ketone 7C	537683
Anisole	108.00	3.54	Aromatic ether	123226

560

561 Fiber optic cables (0.48 na, 400 um core diameter) connected light emitting diodes (465 nm
562 experimental and 405 nm isosbestic excitation wavelengths) to a filter cube that separating excitation
563 and emission wavelengths (Doric). Excitation wavelengths were directed along a fiber optic tether (0.48
564 na, 200 um core diameter) toward the mouse through a rotary connector attached to the behavior box.
565 The same fiber carried emission wavelengths from the mouse to the filter cube, which was then directed
566 to a femtowatt photodetector (Newport) through a fiber optic cable (0.48 na, 600 um core diameter). 405
567 and 465 nm excitations were controlled by Doric Studio software in "lock-in" mode and the emission
568 evoked by each channel was separated into distinct Ca-dependent and isosbestic GCaMP traces in Doric
569 Studio. Traces were then exported to MATLAB where Ca-dependent GCaMP traces were scaled to the
570 isosbestic traces, isosbestic signals were subtracted to remove artifacts, and the subtracted traces were
571 z-scored. Signals were then aligned to odor presentations and subdivided into individual go/no-go trials
572 using the TTL output from the behavior apparatus.

573 Z scored photometry traces from individual trials within a go/no-go session were sorted based on
574 trial type and outcome. Additional realignment of photometry traces based on reward port entry time was
575 carried out in MATLAB using output from MedPC software. Mean traces were calculated for each session
576 by trial type and averaged across animals and sessions. Error was calculated as the 95% confidence
577 interval across sessions. Peak odor response values were calculated as the maximum value of the z
578 scored photometry trace during the odor presentations on individual trials and then averaged across the
579 session. Session averages were then averaged for each animal and mouse-averaged values were
580 compared across trial types using one way ANOVA. For photometric recordings of GCaMP from SST
581 neurons, the area under the curve (AUC) of the reward-related response was calculated for Hit and False
582 Alarm traces by summing the z score from reward port entry to 1 second after reward port entry. For
583 recordings from PV neurons, reward-related suppression was calculated as the sum of the z scored trace
584 from reward port entry to 5 seconds after reward port entry. Values were not calculated for Miss and
585 Correct Reject trials because those trials did not involve reward port entry. For analyses subdividing
586 sessions to examine within-session learning (Figure 2E-H, Figure 4 E-H), traces were extracted from
587 single blocks of 20 trials. The "first block" included the first 20 trials from a session. The "best block" was
588 considered the block of 20 trials with the highest accuracy. If more than one block achieved the same
589 level of high accuracy, traces from the first instance of high accuracy were used. AUC values were then
590 calculated from Hit trials within the "first block" and the "best block" of a session and compared with a
591 paired t-test.

592

593 **Go/no-go testing with DREADD-mediated inhibition**

594 For go/no-go experiments involving DREADD mediated inhibition of SST neurons, odor pairs were
595 presented in the order shown in Table 2. The same odor pairs were presented on consecutive days until
596 mice achieved at least two consecutive blocks of 85% accuracy, when the odor pair was considered

597 learned, or until the mice failed to learn for three consecutive days. Sessions of the same odor pair were
598 then concatenated into a single session spanning up to three days. Concatenated sessions were
599 excluded from analysis if mice failed to complete at least 100 trials. Mice were treated each day, 15
600 minutes before starting the go/no-go task, with either CNO (3.5 mg/kg in 1% DMSO, Tocris) or vehicle
601 (1% DMSO in saline) by I. P. injection. Mice were habituated to I. P. injections of 1% DMSO during the
602 last stage of go/no-go training. CNO or vehicle treatment was consistent within each concatenated
603 session such that each session of the same odor pair (up to three consecutive sessions) was associated
604 with the same drug treatment (Figure 6B). Behavior was quantified using the signal detection theory
605 measures d prime ($d' = Z(Hit\ Rate) - Z(False\ Alarm\ Rate)$) and criterion ($C = -1(Z(Hit\ Rate) +$
606 $Z(False\ Alarm\ Rate))$) (Stanislaw and Todorov, 1999). d' measures the sensitivity of discrimination and
607 reflects overall task performance. C measures discrimination bias. More negative C values reflect a bias
608 towards reward seeking, values close to 0 reflect optimal decision bias, and positive values reflect bias
609 away from reward-seeking, in favor of trial reinitiation. To show change in sensitivity over time within a
610 session, d' was calculated over a rolling window of 40 trials. As an additional control, a subset of mice
611 was injected with a non-DREADD expressing virus (AAV-ef1a-FLEX-mCherry) and subjected to the same
612 experimental paradigm. For experimental and control mice, d' and C were calculated for each odor pair
613 and values were averaged for each mouse separated by treatment condition. Mean values for each
614 mouse from CNO treatment sessions were compared to mean values from vehicle treatment sessions
615 by paired t-tests.

616

617 **Table 2: Odors used in go/no-go experiments with DREADD-mediated inhibition of SST neurons**

Pair #	Odor	S+/S-	Treatment	Cat. Number
1	Anisole	S+	Vehicle	123226
	Acetophenone	S-		200905
2	Isoamyl acetate	S+	CNO	205508
	2-Heptanone	S-		537683
3	2-Methypyrazine	S+	Vehicle	75608
	alpha-Pinene	S-		147524
4	(+) Carvone	S+	CNO	124931
	(-) Carvone	S-		22070
5	(+) Limonene	S+	Vehicle	183164
	(-) Limonene	S-		218367
6	2-Ethylphenol	S+	CNO	44000
	1,4-Cineole	S-		27393
7	1-Butenol	S+	Vehicle	281549
	1-Pentanol	S-		138975
8	1-Hexanol	S+	CNO	H13303
	1-Heptanol	S-		H2805
9	2,3 Hexanendione	S+	Vehicle	255801
	Citral	S-		83007
10	Isoamyl Butyrate	S+	CNO	206008
	Menthone	S-		218235

618

619 **Electrophysiology**

620 For slice electrophysiological recording experiments, mice (N = 3) were deeply anesthetized with
621 isoflurane then transcardially perfused with ice-cold artificial cerebrospinal fluid (aCSF) solution
622 containing (in mM): 125 NaCl, 2.5 KCl, 1.25 NaH2P04, 1 MgCl2, 2 CaCl2, 25 glucose, and 25
623 bicarbonate (pH 7.3, 295 mOsM). Brains were removed and transferred into ice-cold cutting solution
624 containing (in mM): 2.5 KCl, 1.25 NaH2PO4, 10 MgSO4, 0.5 CaCl2, 234 sucrose, 11 glucose, and 26
625 bicarbonate. Cutting solution was continuously bubbled with 95% CO2 / 5% O2. Brains were mounted
626 with cyanoacrylate glue and immediately submerged in oxygenated cutting solution on a Leica VT1200
627 vibratome. 300 um coronal sections were made at a cutting speed of 0.1 mm/s. Slices including the
628 HDB were removed to a slice recovery chamber of oxygenated aCSF at 37C for at least 30 minutes.
629 Following recovery, slices were slowly returned to room temperature for 30 minutes before recording.

630 For whole-cell current clamp recordings, slices were submerged in a recording chamber and
631 continuously perfused with room temperature oxygenated aCSF at ~2 mL/minute. Cells were visualized
632 with DIC optics (Olympus BX50WI) and fluorescence imaging (Q Capture). Once visualized, cells were
633 whole-cell patched in current-clamp configuration. Recording electrodes (3–7 megaohms) were pulled

634 from thin-walled borosilicate glass capillaries (inner diameter: 1.1 mm, outer diameter: 1.5 mm) with a
635 horizontal micropipette puller (Sutter Instruments). Current-clamp internal solution contained (in mM):
636 120 K gluconate, 20 HEPES, 10 EGTA, 2 MgATP, and 0.2 NaGTP (with 0.4% biocytin by weight, pH to
637 7.3 with KOH, 285 mOsM). Recordings were made using PClamp software (Axon) with an Axon
638 MultiClamp 700B amplifier digitized at 10 kHz (Axon Digidata 1440A). Once a whole cell patch was
639 achieved, cells were allowed to equilibrate for five minutes before resting membrane potential was
640 recorded and current injections were performed. Cells were then injected with 1 s current steps from -
641 100 pA to +180 pA in intervals of 20 pA. Resting membrane potential was recorded and current
642 injections were repeated three times. After recording current injections at baseline, CNO (10 uM) was
643 washed added to the bath and allowed to circulate for 10 minutes. Resting membrane potential was
644 recorded and current injections were repeated three times in the presence of CNO. During all
645 recordings, access resistance was continuously monitored, and cells where the access resistance
646 changed by more than 20% were excluded from analysis. N = 5 fluorescently labeled cells and N = 7
647 unlabeled cells. Traces were then exported to MATLAB where resting membrane potential and spike
648 counts were calculated with custom scripts.

649 All cells were dialyzed with 0.4% biocytin for the duration of the recording and patched neurons
650 were saved for post hoc imaging. After recordings, electrodes were withdrawn slowly allowing the cells
651 to reseal and form an outside-out patch. Slices were then allowed to equilibrate in the recording
652 chamber for 5 minutes before being transferred to 4% PFA. After patching and cell-filling, slices were
653 fixed overnight in 4% PFA at 4º C. Slices were then washed 3x in 0.1% PBS-T for 30 min each. After
654 washing, slices were incubated in 10% normal goat serum blocking buffer for 2 hours at room
655 temperature. Slices were then incubated in streptavidin conjugated to Alexa:647 (1:500, Invitrogen)
656 overnight at 4C. The next day, slices were washed 3x in 0.1% PBS-T for 30 min, then mounted on
657 glass slides using 500 um spacers (Electron Microscopy Sciences) filled with mounting media without
658 DAPI (Southern Biotech). Slices were imaged on a Leica SP8 confocal with a 20x objective to verify
659 colocalization with DREADD expression. Z stacks of filled cells were reconstructed in FIJI.

660

661 **Immunofluorescence and imaging**

662 For antibody staining of GCaMP in mice used for photometry experiments, mice were deeply
663 anesthetized then transcardially perfused with PBS followed by 4% PFA. Brains were removed and
664 immersion fixed in 4% PFA overnight at 4C. Brains were transferred to 30% sucrose and allowed to
665 equilibrate, then they were frozen and sectioned at 40 um on a cryostat (Leica). Sections were washed
666 in 0.3% PBS-T, then incubated in a blocking solution composed of 10% normal goat serum, 0.3% PBS-
667 T, and 3M glycine for 1 hour at room temperature. Following blocking, slices were incubated in primary
668 antibody (Chicken a GFP, 1:1000, Abcam, ab13970) diluted in blocking buffer overnight at 4C. The next
669 day slices were washed 3x in 0.1% PBS-T then incubated in secondary antibody (Goat a Chicken:488,

670 1:1000, Invitrogen, A32931) for 2 hours at room temperature. Slices were then washed 3x in 0.3%
671 PBS-T, transferred to 0.5x PBS, and mounted on glass slides with DAPI-containing mounting media
672 (Southern Biotech). For fluorescence imaging of DREADD-mCherry expression, the endogenous
673 mCherry fluorescence was sufficient for imaging and no antibody staining was performed. Sections
674 were imaged on a Leica DM6000B epifluorescence microscope. For characterization of DREADD
675 expression in mice used for behavioral experiments (Figure 6), three equivalent sections including the
676 HDB/MCPO/SI complex were selected from each mouse and the region of viral expression was
677 outlined manually in FIJI and superimposed onto the matching coronal section schematic (Figure 6A).

678

679 **Statistics and Data Analysis**

680 All statical analyses were caried out with Prism software (Graphpad). For comparisons across four trial
681 types where values were matched by animal and session, repeated measures one-way ANOVAs were
682 used. For comparisons across two trial types or groups where values were matched by animal and
683 session, paired t tests were used. For comparisons to a null hypothesis value, one sample t tests were
684 used. When mouse average values are reported, overall averages and errors are calculated from
685 mouse average values. For correlation analyses, correlations are reported as Pearson's R values.
686 Lines of best fit, confidence intervals, slopes, intercepts, and significance values in were calculated with
687 simple linear regressions for each trial type separately. For analyses comparing CNO and vehicle
688 treatment in control and experimental animals paired t tests were used separately for control and
689 experimental groups.

690 **REFERENCES**

691 Agostinelli LJ, Geerling JC, Scammell TE (2019) Basal forebrain subcortical projections. Brain Struct
692 Funct 224:1097–1117.
693 Anaclet C, de Luca R, Venner A, Malyshevskaya O, Lazarus M, Arrigoni E, Fuller PM (2018) Genetic
694 activation, inactivation, and deletion reveal a limited and nuanced role for somatostatin-
695 containing basal forebrain neurons in behavioral state control. Journal of Neuroscience 38:5168–
696 5181.
697 Anaclet C, Pedersen NP, Ferrari LL, Venner A, Bass CE, Arrigoni E, Fuller PM (2015) Basal forebrain
698 control of wakefulness and cortical rhythms. Nat Commun 6:8744.
699 Ballinger EC, Ananth M, Talmage DA, Role LW (2016) Basal forebrain cholinergic circuits and signaling in
700 cognition and cognitive decline. Neuron 91:1199–1218.
701 Bendahmane M, Ogg MC, Ennis M, Fletcher ML (2016) Increased olfactory bulb acetylcholine bi-
702 directionally modulates glomerular odor sensitivity. Sci Rep 6:1–13.
703 Bigl V, Woolf NJ, Butcher LL (1982) Cholinergic projections from the basal forebrain to frontal, parietal,
704 temporal, occipital, and cingulate cortices: a combined fluorescent tracer and
705 acetylcholinesterase analysis. Brain Res Bull 8:727–749.
706 Böhm E, Brunert D, Rothermel M (2020) Input dependent modulation of olfactory bulb activity by HDB
707 GABAergic projections. Sci Rep 10:1–15.
708 Castillo PE, Carleton A, Vincent J-D, Lledo P-M (1999) Multiple and opposing roles of cholinergic
709 transmission in the main olfactory bulb. Journal of Neuroscience 19:9180–9191.
710 Chaudhury D, Escanilla O, Linster C (2009) Bulbar acetylcholine enhances neural and perceptual odor
711 discrimination. Journal of Neuroscience 29:52–60.
712 Chaves-Coira I, Barros-Zulaica N, Rodrigo-Angulo M, Núñez Á (2016) Modulation of specific sensory
713 cortical areas by segregated basal forebrain cholinergic neurons demonstrated by neuronal
714 tracing and optogenetic stimulation in mice. Front Neural Circuits 10:28.
715 de Saint Jan D (2022) Target-specific control of olfactory bulb periglomerular cells by GABAergic and
716 cholinergic basal forebrain inputs. Elife 11:e71965.
717 Devore S, Pender-Morris N, Dean O, Smith D, Linster C (2015) Basal forebrain dynamics during
718 nonassociative and associative olfactory learning. J Neurophysiol 115:423–433.
719 Do JP, Xu M, Lee S-H, Chang W-C, Zhang S, Chung S, Yung TJ, Fan JL, Miyamichi K, Luo L (2016) Cell
720 type-specific long-range connections of basal forebrain circuit. Elife 5:e13214.
721 Elaagouby A, Ravel N, Gervais R (1991) Cholinergic modulation of excitability in the rat olfactory bulb:
722 effect of local application of cholinergic agents on evoked field potentials. Neuroscience 45:653–
723 662.
724 Fisher RS, Buchwald NA, Hull CD, Levine MS (1988) GABAergic basal forebrain neurons project to the
725 neocortex: the localization of glutamic acid decarboxylase and choline acetyltransferase in feline
726 corticopetal neurons. Journal of Comparative Neurology 272:489–502.
727 Gielow MR, Zaborszky L (2017) The input-output relationship of the cholinergic basal forebrain. Cell
728 Rep 18:1817–1830.
729 Goard M, Dan Y (2009) Basal forebrain activation enhances cortical coding of natural scenes. Nat
730 Neurosci 12:1444–1449.
731 Gracia-Llanes FJ, Crespo C, Blasco-Ibáñez JM, Nacher J, Varea E, Rovira-Esteban L, Martínez-Guijarro FJ
732 (2010) GABAergic basal forebrain afferents innervate selectively GABAergic targets in the main
733 olfactory bulb. Neuroscience 170:913–922.
734 Gritton HJ, Howe WM, Mallory CS, Hetrick VL, Berke JD, Sarter M (2016) Cortical cholinergic signaling
735 controls the detection of cues. Proceedings of the National Academy of Sciences 113:E1089–
736 E1097.

737 Grothe M, Zaborszky L, Atienza M, Gil-Neciga E, Rodriguez-Romero R, Teipel SJ, Amunts K, Suarez-
738 Gonzalez A, Cantero JL (2010) Reduction of basal forebrain cholinergic system parallels cognitive
739 impairment in patients at high risk of developing Alzheimer's disease. Cerebral Cortex 20:1685–
740 1695.
741 Hangya B, Ranade SP, Lorenc M, Kepecs A (2015) Central cholinergic neurons are rapidly recruited by
742 reinforcement feedback. Cell 162:1155–1168.
743 Hanson E, Brandel-Ankrapp KL, Arenkiel BR (2021) Dynamic cholinergic tone in the basal forebrain
744 reflects reward-seeking and reinforcement during olfactory behavior. Front Cell Neurosci
745 15:635837.
746 Hanson E, Swanson J, Arenkiel BR (2020) GABAergic Input From the Basal Forebrain Promotes the
747 Survival of Adult-Born Neurons in the Mouse Olfactory Bulb. Front Neural Circuits 14.
748 Harrison TC, Pinto L, Brock JR, Dan Y (2016) Calcium imaging of basal forebrain activity during innate
749 and learned behaviors. Front Neural Circuits 10:36.
750 Hassani OK, Lee MG, Henny P, Jones BE (2009) Discharge profiles of identified GABAergic in
751 comparison to cholinergic and putative glutamatergic basal forebrain neurons across the sleep–
752 wake cycle. Journal of Neuroscience 29:11828–11840.
753 Hasselmo ME (1999) Neuromodulation: acetylcholine and memory consolidation. Trends Cogn Sci
754 3:351–359.
755 Hasselmo ME, McGaughy J (2004) High acetylcholine levels set circuit dynamics for attention and
756 encoding and low acetylcholine levels set dynamics for consolidation. Prog Brain Res 145:207–
757 231.
758 Herman AM, Ortiz-Guzman J, Kochukov M, Herman I, Quast KB, Patel JM, Tepe B, Carlson JC, Ung K,
759 Selever J (2016) A cholinergic basal forebrain feeding circuit modulates appetite suppression.
760 Nature 538:253–256.
761 Herrero JL, Roberts MJ, Delicato LS, Gieselmann MA, Dayan P, Thiele A (2008) Acetylcholine
762 contributes through muscarinic receptors to attentional modulation in V1. Nature 454:1110–
763 1114.
764 Kim T, Thankachan S, McKenna JT, McNally JM, Yang C, Choi JH, Chen L, Kocsis B, Deisseroth K, Strecker
765 RE, Basheer R, Brown RE, McCarley RW (2015) Cortically projecting basal forebrain parvalbumin
766 neurons regulate cortical gamma band oscillations. Proceedings of the National Academy of
767 Sciences 112:201413625.
768 Lau B, Salzman CD (2008) Noncholinergic neurons in the basal forebrain: often neglected but
769 motivationally salient. Neuron 59:6–8.
770 Ledbetter NM, Chen CD, Monosov IE (2016) Multiple mechanisms for processing reward uncertainty in
771 the primate basal forebrain. Journal of Neuroscience 36:7852–7864.
772 Levin ED, Simon BB (1998) Nicotinic acetylcholine involvement in cognitive function in animals.
773 Psychopharmacology (Berl) 138:217–230.
774 Lin S-C, Nicolelis MAL (2008) Neuronal ensemble bursting in the basal forebrain encodes salience
775 irrespective of valence. Neuron 59:138–149.
776 Ma M, Luo M (2012) Optogenetic Activation of Basal Forebrain Cholinergic Neurons Modulates
777 Neuronal Excitability and Sensory Responses in the Main Olfactory Bulb. The Journal of
778 Neuroscience 32:10105–10116.
779 Mandairon N, Ferretti CJ, Stack CM, Rubin DB, Cleland TA, Linster C (2006) Cholinergic modulation in
780 the olfactory bulb influences spontaneous olfactory discrimination in adult rats. European Journal
781 of Neuroscience 24:3234–3244.
782 Markram H, Segal M (1990) Long-lasting facilitation of excitatory postsynaptic potentials in the rat
783 hippocampus by acetylcholine. J Physiol 427:381–393.

McDonald AJ, Muller JF, Mascagni F (2011) Postsynaptic targets of GABAergic basal forebrain projections to the basolateral amygdala. Neuroscience 183:144–159.

Muir JL, Page KJ, Sirinathsinghji DJS, Robbins TW, Everitt BJ (1993) Excitotoxic lesions of basal forebrain cholinergic neurons: effects on learning, memory and attention. Behavioural brain research 57:123–131.

Nunez-Parra A, Maurer RK, Krahe K, Smith RS, Araneda RC (2013) Disruption of centrifugal inhibition to olfactory bulb granule cells impairs olfactory discrimination. Proceedings of the National Academy of Sciences 110:14777–14782.

Nunez-Parra A, Rio C-D, Christian A, Huntsman MM, Restrepo D (2020) The basal forebrain modulates neuronal response in an active olfactory discrimination task. Front Cell Neurosci 14:141.

Ogg MC, Ross JM, Bendahmane M, Fletcher ML (2018) Olfactory bulb acetylcholine release dishabituates odor responses and reinstates odor investigation. Nat Commun 9:1–11.

Parikh V, Kozak R, Martinez V, Sarter M (2007) Prefrontal acetylcholine release controls cue detection on multiple timescales. Neuron 56:141–154.

Parrao T, Chana P, Venegas P, Behrens MI, Aylwin ML (2012) Olfactory deficits and cognitive dysfunction in Parkinson's disease. Neurodegener Dis 10:179–182.

Patel JM, Swanson J, Ung K, Herman A, Hanson E, Ortiz-Guzman J, Selever J, Tong Q, Arenkiel BR (2019) Sensory perception drives food avoidance through excitatory basal forebrain circuits. Elife 8.

Phillis JW (1968) Acetylcholine release from the cerebral cortex: its role in cortical arousal. Brain Res 7:378–389.

Pinto L, Goard MJ, Estandian D, Xu M, Kwan AC, Lee S-H, Harrison TC, Feng G, Dan Y (2013) Fast modulation of visual perception by basal forebrain cholinergic neurons. Nat Neurosci 16:1857–1863.

Rothermel M, Carey RM, Puche A, Shipley MT, Wachowiak M (2014) Cholinergic inputs from Basal forebrain add an excitatory bias to odor coding in the olfactory bulb. Journal of Neuroscience 34:4654–4664.

Rothermel M, Wachowiak M (2014) Functional imaging of cortical feedback projections to the olfactory bulb. Front Neural Circuits 8:73.

Ruivo LMT-G, Baker KL, Conway MW, Kinsley PJ, Gilmour G, Phillips KG, Isaac JTR, Lowry JP, Mellor JR (2017) Coordinated acetylcholine release in prefrontal cortex and hippocampus is associated with arousal and reward on distinct timescales. Cell Rep 18:905–917.

Sanz Diez A, Najac M, De Saint Jan D (2019) Basal forebrain GABAergic innervation of olfactory bulb periglomerular interneurons. J Physiol 597:2547–2563.

Sarter M, Bruno JP (1997) Cognitive functions of cortical acetylcholine: toward a unifying hypothesis. Brain Res Rev 23:28–46.

Sarter M, Bruno JP (1999) Cortical cholinergic inputs mediating arousal, attentional processing and dreaming: differential afferent regulation of the basal forebrain by telencephalic and brainstem afferents. Neuroscience 95:933–952.

Sarter M, Bruno JP, Turchi J (1999) Basal forebrain afferent projections modulating cortical acetylcholine, attention, and implications for neuropsychiatric disorders. Ann N Y Acad Sci 877:368–382.

Sarter M, Givens B, Bruno JP (2001) The cognitive neuroscience of sustained attention: where top-down meets bottom-up. Brain Res Rev 35:146–160.

Semba K (1991) The cholinergic basal forebrain: a critical role in cortical arousal. The basal forebrain:197–218.

Stanislaw H, Todorov N (1999) Calculation of signal detection theory measures. Behavior research methods, instruments, & computers 31:137–149.

Szymusiak R (1995) Magnocellular nuclei of the basal forebrain: substrates of sleep and arousal regulation. Sleep 18:478–500.

Szymusiak R, Alam N, McGinty D (2000) Discharge patterns of neurons in cholinergic regions of the basal forebrain during waking and sleep. Behavioural brain research 115:171–182.

Tashakori-Sabzevar F, Ward RD (2018) Basal forebrain mediates motivational recruitment of attention by reward-associated cues. Front Neurosci 12:786.

Tingley D, Alexander AS, Quinn LK, Chiba AA, Nitz DA (2015) Cell assemblies of the basal forebrain. Journal of Neuroscience 35:2992–3000.

Tsuno Y, Kashiwadani H, Mori K (2008) Behavioral state regulation of dendrodendritic synaptic inhibition in the olfactory bulb. Journal of Neuroscience 28:9227–9238.

Villar PS, Hu R, Araneda RC (2020) Long-range GABAergic inhibition modulates spatiotemporal dynamics of the output neurons in the olfactory bulb. bioRxiv.

Woolf NJ, Hernit MC, Butcher LL (1986) Cholinergic and non-cholinergic projections from the rat basal forebrain revealed by combined choline acetyltransferase and Phaseolus vulgaris leucoagglutinin immunohistochemistry. Neurosci Lett 66:281–286.

Xu M, Chung S, Zhang S, Zhong P, Ma C, Chang W-C, Weissbourd B, Sakai N, Luo L, Nishino S (2015) Basal forebrain circuit for sleep-wake control. Nat Neurosci 18:1641–1647.

Zaborszky L, Carlsen J, Brashear HR, Heimer L (1986) Cholinergic and GABAergic afferents to the olfactory bulb in the rat with special emphasis on the projection neurons in the nucleus of the horizontal limb of the diagonal band. Journal of Comparative Neurology 243:488–509.

Zaborszky L, Duque A (2000a) Local synaptic connections of basal forebrain neurons. Behavioural brain research 115:143–158.

Zaborszky L, Duque A (2000b) Local synaptic connections of basal forebrain neurons. Behavioural brain research 115:143–158.

Zant JC, Kim T, Prokai L, Szarka S, McNally J, McKenna JT, Shukla C, Yang C, Kalinchuk A v, McCarley RW (2016) Cholinergic neurons in the basal forebrain promote wakefulness by actions on neighboring non-cholinergic neurons: an opto-dialysis study. Journal of Neuroscience 36:2057–2067.

Zhang K, Chen CD, Monosov IE (2019) Novelty, salience, and surprise timing are signaled by neurons in the basal forebrain. Current Biology 29:134–142.

Zheng Y, Feng S, Zhu X, Jiang W, Wen P, Ye F, Rao X, Jin S, He X, Xu F (2018) Different subgroups of cholinergic neurons in the basal forebrain are distinctly innervated by the olfactory regions and activated differentially in olfactory memory retrieval. Front Neural Circuits 12:99.

Zheng Y, Tao S, Liu Y, Liu J, Sun L, Zheng Y, Tian Y, Su P, Zhu X, Xu F (2022) Basal Forebrain-Dorsal Hippocampus Cholinergic Circuit Regulates Olfactory Associative Learning. Int J Mol Sci 23:8472.

Figure 1: Basal forebrain PV neurons are excited by odor and suppressed by reward delivery

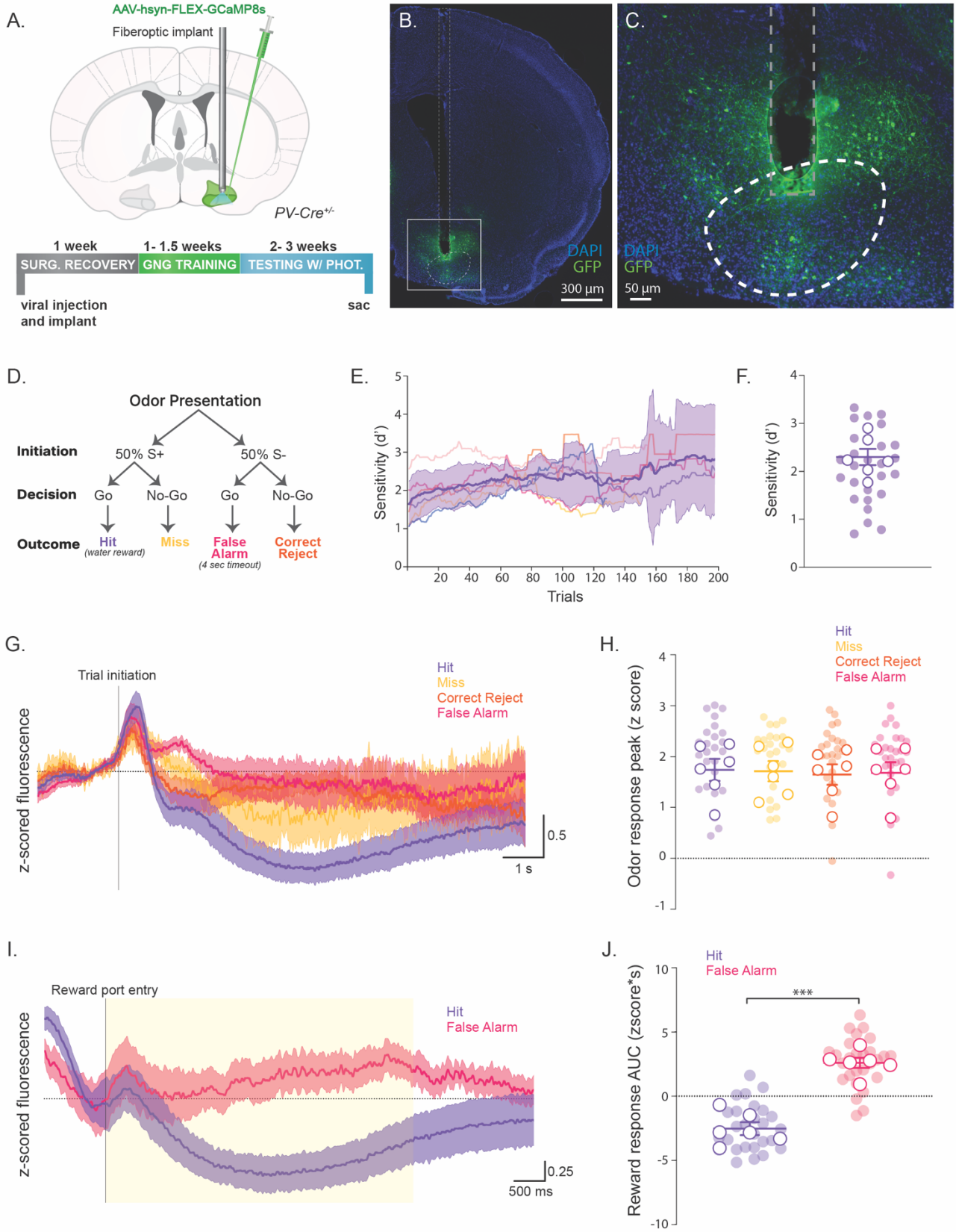

867

868 **Figure 1: BF PV neurons are excited by odor and suppressed by reward delivery. A.** Schematic
869 showing injection of Cre-dependent viral construct and fiberoptic implant in PV-Cre mice (top).
870 Highlighted regions of the BF include the horizontal limb of the diagonal band of broca (HDB), the
871 magnocellular preoptic nucleus (MCPO) and substantia innominata (SI). An experimental timeline
872 shows timing of surgery, behavioral training, and behavioral testing with fiber photometry imaging
873 (bottom). **B.** Example slice image showing the implant tract and expression of GCaMP. **C.** Viral
874 expression and implant tip localization in the HDB. **D.** Schematic of olfactory-cued go/no-go behavioral
875 paradigm showing possible stimuli, decisions, and outcomes of individual trials. **E.** Performance of
876 mice in the testing phase quantified as a rolling window of sensitivity (d') across trials. Averages of all
877 sessions (n = 26) for individual mice (N = 6) are shown as single lines. Average across mice is overlaid
878 (purple line) with 95% confidence intervals (shaded purple). **F.** Average d' for individual sessions
879 (purple circles) and mouse averages (white circles) with mean and SEM of mouse averages. **G.**
880 Average z-scored GCaMP traces of the four trial types listed in D overlaid with 95% confidence
881 intervals (shaded regions). **H.** Peak signal amplitudes of the four trial types. Pastel circles represent the
882 peak odor response of each testing session. White circles represent the average peak odor response of
883 each animal. Line shows mean across animals. Error bars show SEM across animals. **I.** Average z-
884 scored GCaMP traces for Hit and False Alarm trials aligned to the time of reward port entry with 95%
885 confidence intervals overlaid (shaded regions). Yellow shaded area represents the time over which the
886 area under the curve (AUC) was quantified. **J.** Area under the curve (AUC) of Hit and False Alarm
887 traces across testing sessions. Transparent circles represent the AUC of each testing session. White
888 circles represent the average AUC of each animal. Lines show mean across animals and error bars
889 show SEM across animals. *** $p < 0.001$ paired t test across N = 6 animals.

Figure 2: PV neuron odor and reward responses correlated with go/no-go task performance

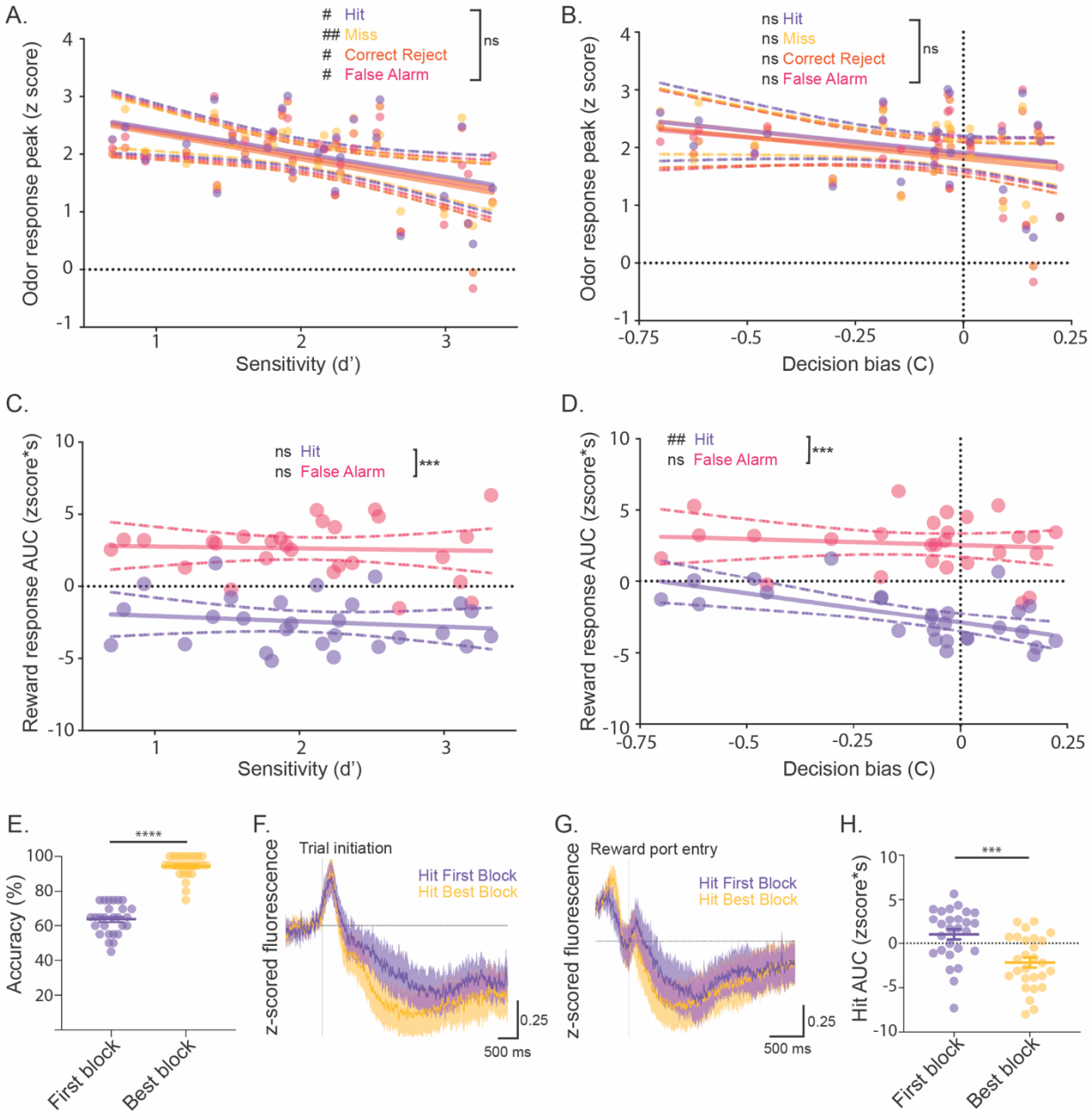

890

Figure 2: PV neuron odor and reward responses are correlated with go/no-go task performance. **A.** Correlation of the peak odor responses with discrimination sensitivity (d') by trial type, across sessions. Circles show values of odor response peaks for all trials of a given type within a session plotted against the d' value for that session. Lines of best fit (solid lines) are shown for each trial type with 95% confidence intervals (dashed lines). Hash tags indicate slopes of best fit lines that are significantly different from zero. # $p < 0.05$, ## $p < 0.01$. Bracketed n.s. indicates that no best fit line slopes are significantly different from each other. **B.** Correlation of peak odor response with decision bias (C) by trial types across sessions. Circles show values of odor response peaks for all trials of a given type within a session plotted against the C value for that session. Lines of best fit (solid lines) are shown for each trial type with 95% confidence intervals (dashed lines). Bracketed and individual trial type n.s. indicates that no best fit line slopes are significantly different from each other or from zero. **C.** Correlation of the reward response area under the curve (AUC) with discrimination sensitivity (d') by reward seeking trial type, across sessions. Circles show values of odor response peaks for hit and false alarm trials within a session plotted against the d' value for that session. Lines of best fit (solid lines) are shown for each trial type with 95% confidence intervals (dashed lines). Slopes of each best fit line are not significantly different from zero (n.s.). Bracketed asterisks indicate a significant difference between the y intercepts of the best fit lines (*** $p < 0.001$). **D.** Correlation of the reward response AUC with decision bias (C) by reward seeking trial type. Circles show values of odor response peaks for hit and false alarm trials within a session plotted against the C value for that session. Lines of best fit (solid lines) are shown for each trial type with 95% confidence intervals (dashed lines). Hash tags indicate a best fit line slope significantly different from zero (## $p < 0.01$). Bracketed asterisks indicate a significant difference between the y intercepts of the best fit lines (*** $p < 0.001$). **E.** Accuracy (% correct trials) from first block of 20 trials in a session (purple) compared to the block of 20 trials with highest accuracy in a session (yellow). Circles show values for individual sessions with lines and error bars showing mean and SEM. **** $p < 0.0001$, paired t test. **F.** Average traces (solid lines), aligned to the time of odor port entry (trial initiation), from hit trials in first blocks (purple) and highest accuracy blocks (yellow) with 95% confidence intervals (shaded regions). Horizontal line indicates baseline subtracted z score = 0. **G.** Average traces (solid lines), aligned to the time of reward port entry, from hit trials in first blocks (purple) and highest accuracy blocks (yellow) with 95% confidence intervals (shaded regions). Horizontal line indicates baseline subtracted z score = 0. **H.** Quantification of the reward-related response (AUC) in hit trials from first (purple) and best blocks (yellow). Circles show values for individual sessions with lines and error bars showing mean and SEM. *** $p < 0.001$.

Figure 3: Basal forebrain SST neurons are excited by odor and reward delivery

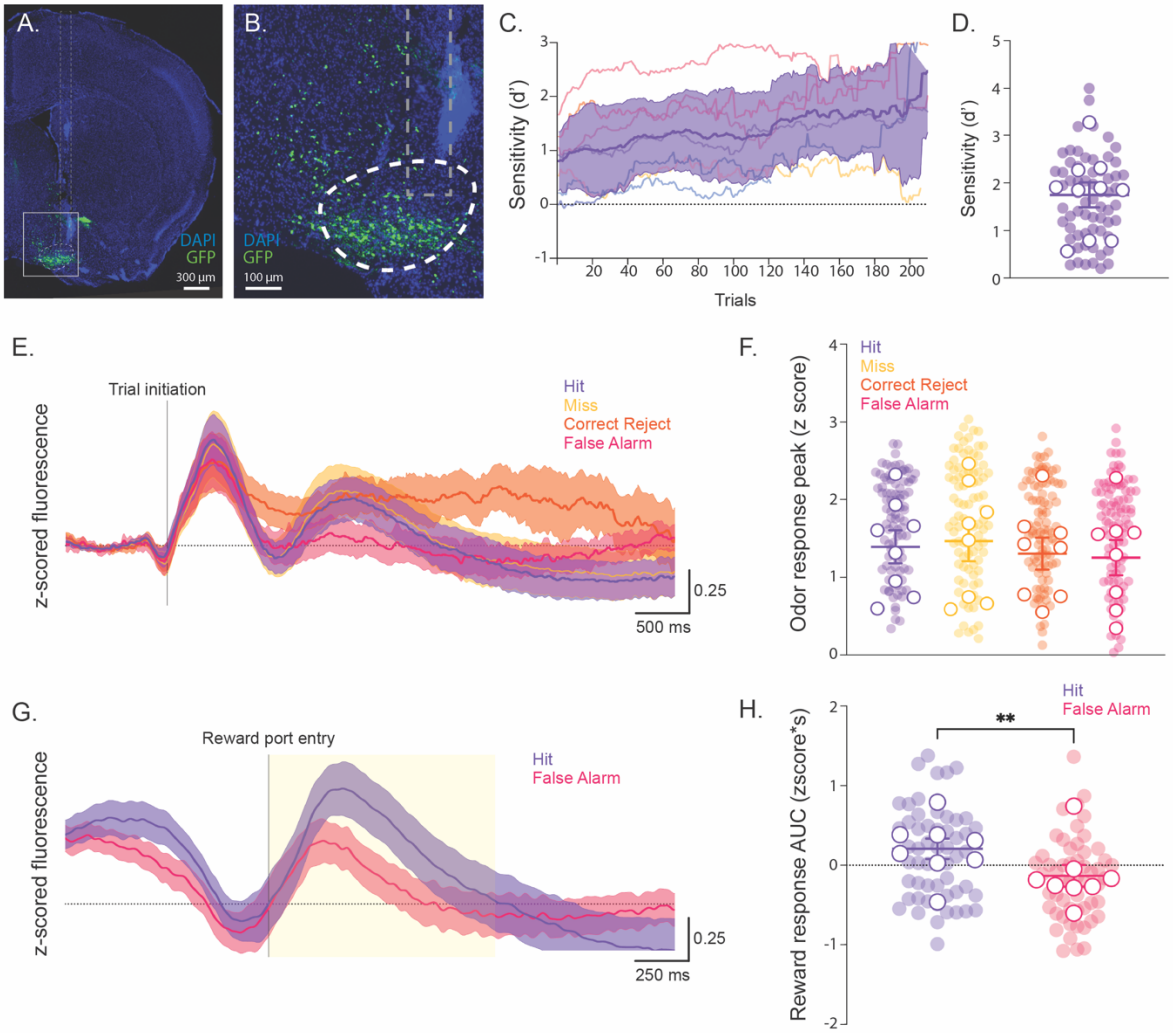

923

Figure 3: BF SST neurons are excited by odor and reward delivery. A. Example slice image showing the implant tract and expression of GCaMP in the BF. **B.** Viral expression and fiberoptic implant tip localization in the HDB. **C.** Performance of mice in the testing phase quantified as a rolling window of sensitivity (d') across trials. Averages of all sessions (n = 50) for individual mice (N = 8) are shown as single lines. Average across mice is overlaid (purple line) with 95% confidence intervals (shaded purple). **D.** Average d' for individual sessions (purple circles) and mouse averages (white circles) with mean and SEM of mouse averages. **E.** Average z-scored GCaMP traces of the four trial types across all sessions overlaid with 95% confidence intervals (shaded regions). **F.** Peak signal amplitudes of the four trial types. Light circles represent the peak odor response of each testing session. White circles represent the average peak odor response of each animal with mean and SEM of mouse averages. **G.** Average z-scored GCaMP traces for Hit and False Alarm trials, aligned to the time of reward port entry, with 95% confidence intervals (shaded regions). Yellow shaded area represents the time over which the area under the curve (AUC) of the reward response was calculated. **H.** Area under the curve (AUC) of Hit and False Alarm traces across testing sessions. Transparent circles represent the AUC of each testing session. White circles represent the average AUC of each animal with mean and SEM of mouse averages. ** $p < 0.01$ paired t test across N = 8 animals.

Figure 4: Basal forebrain SST activity changes with go/no-go task performance and learning

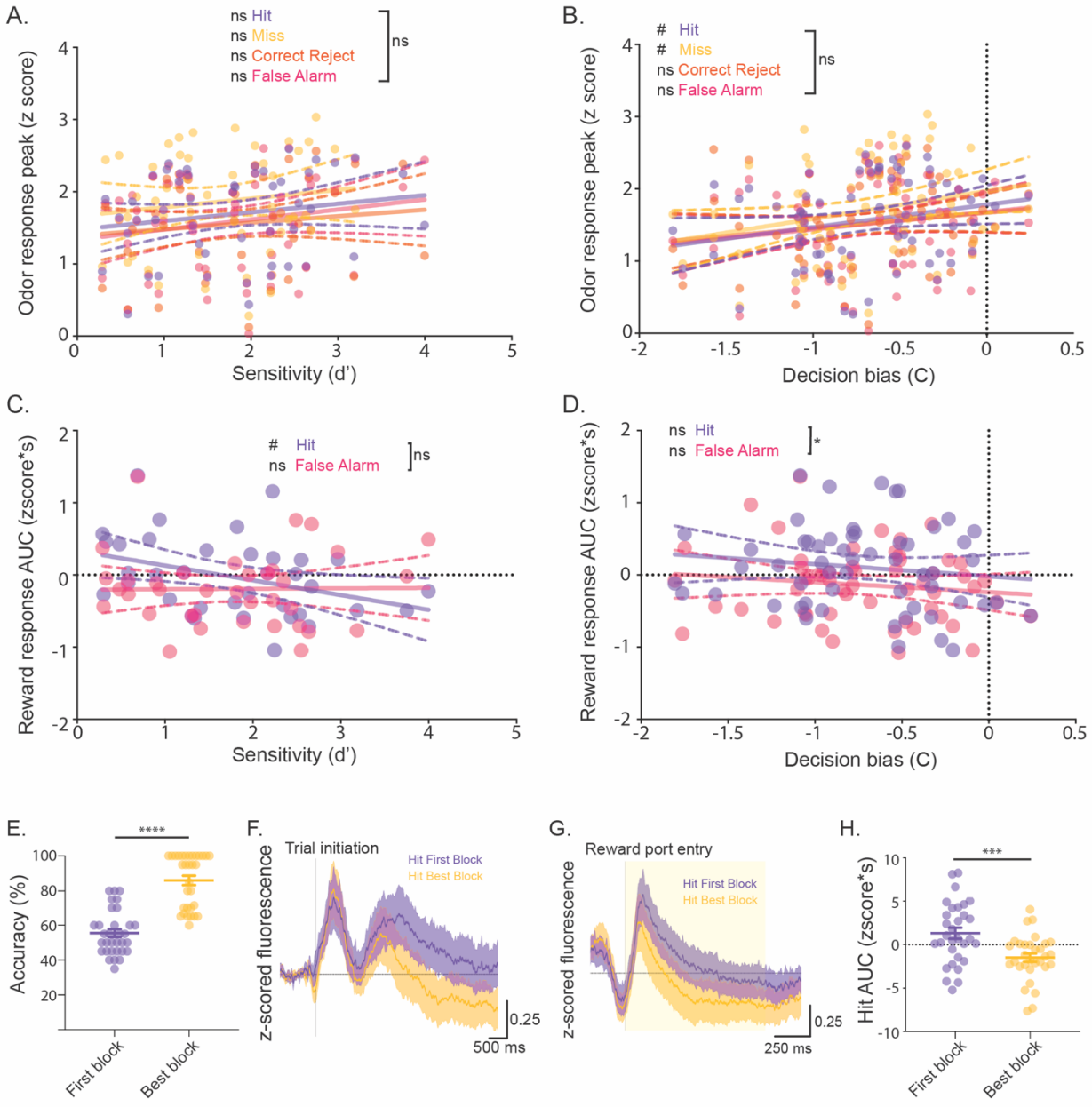

940

Figure 4: BF SST activity changes with go/no-go task performance and learning. A. Correlation of the peak odor responses with discrimination sensitivity (d') by trial type, across sessions. Circles show values of odor response peaks for all trials of a given type within a session plotted against the d' value for that session. Lines of best fit (solid lines) are shown for each trial type with 95% confidence intervals (dashed lines). Bracketed and individual trial type n.s. indicates that no best fit line slopes are significantly different from each other or from zero. **B.** Correlation of peak odor response with decision bias (C) by trial types across sessions. Circles show values of odor response peaks for all trials of a given type within a session plotted against the C value for that session. Lines of best fit (solid lines) are shown for each trial type with 95% confidence intervals (dashed lines). Hash tags indicate a best fit line slope significantly different from zero (# $p < 0.05$). Bracketed n.s. indicates that no best fit line slopes are significantly different from each other. **C.** Correlation of the reward response area under the curve (AUC) with discrimination sensitivity (d') by reward seeking trial type, across sessions. Circles show values of odor response peaks for hit and false alarm trials within a session plotted against the d' value for that session. Lines of best fit (solid lines) are shown for each trial type with 95% confidence intervals (dashed lines). Hash tag indicates a best fit line slope significantly different from zero (# $p < 0.05$). Slopes of each best fit line are not significantly different from each other (bracketed n.s.). **D.** Correlation of the reward response AUC with decision bias (C) by reward seeking trial type. Circles show values of odor response peaks for hit and false alarm trials within a session plotted against the C value for that session. Lines of best fit (solid lines) are shown for each trial type with 95% confidence intervals (dashed lines). Slopes of each best fit line are not significantly different from zero (n.s.). Bracketed asterisk indicates a significant difference between the y intercepts of the best fit lines (* $p < 0.05$). **E.** Accuracy (% correct trials) from first block of 20 trials in a session (purple) compared to the block of 20 trials with highest accuracy in a session (yellow). Circles show values for individual sessions with lines and error bars showing mean and SEM. **** $p < 0.0001$, paired t test. **F.** Average traces (solid lines), aligned to the time of odor port entry (trial initiation), from hit trials in first blocks (purple) and highest accuracy blocks (yellow) with 95% confidence intervals (shaded regions). Horizontal line indicates baseline subtracted z score = 0. **G.** Average traces (solid lines), aligned to the time of reward port entry, from hit trials in first blocks (purple) and highest accuracy blocks (yellow) with 95% confidence intervals (shaded regions). Horizontal line indicates baseline subtracted z score = 0. **H.** Quantification of the reward-related response (AUC) in hit trials from first (purple) and best blocks (yellow). Circles show values for individual sessions with lines and error bars showing mean and SEM. *** $p < 0.001$.

Figure 5: DREADD inhibition of SST neurons in slice does not impact firing of neighboring basal forebrain neurons

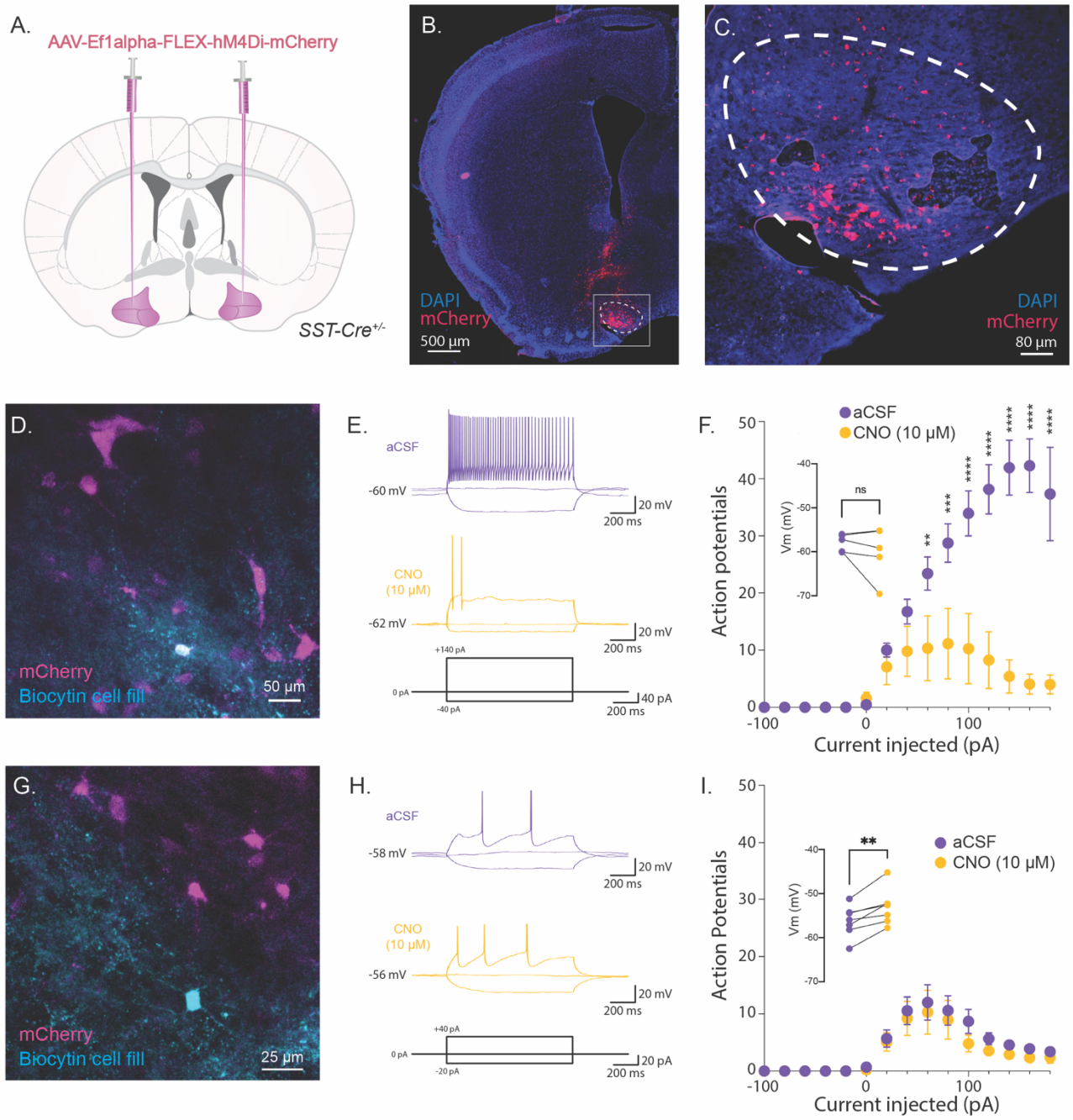

973

Figure 5: DREADD inhibition of SST neurons in slice does not impact firing of neighboring BF neurons. A. Schematic showing bilateral injection of Cre-dependent hM4Di viral construct into basal forebrain regions including the horizontal limb of the diagonal band of broca (HDB), magnocellular preoptic nucleus (MCPO), and substantia innominata (SI) of SST-Cre mice. **B.** Example of hM4Di-mCherry expression in BF with the HDB outlined. **C.** Inset from B showing hM4Di-mCherry expression in HDB. **D.** Example cell fill and hM4Di-mCherry expression from patched hM4Di-expressing (mCherry+) SST neuron. **E.** Example responses to current injections in aCSF (top, purple) and after CNO (10 μM) wash on (yellow middle). Bottom panel shows current injection schematic for example traces. Traces are from cell shown in D. **F.** For hM4Di-expressing neurons: Quantification of action potentials fired at each current injection in aCSF (purple) and after CNO wash on (yellow). n = 5 cells. Circles show mean ± SEM. ** $p < 0.01$, *** $p < 0.001$, **** $p < 0.0001$, paired t test. Inset shows resting membrane potential of each cell before (purple) and after (yellow) wash on of CNO. **G.** Example cell fill and hM4Di-mCherry expression from patched neuron not expressing hM4Di. **H.** Example responses to current injections in aCSF (top, purple) and after CNO (10 μM) wash on (yellow middle). Bottom panel shows current injection schematic for example traces. Traces are from cell shown in G. **I.** For patched neurons not expressing hM4Di: Quantification of action potentials fired at each current injection in aCSF (purple) and after CNO wash on (yellow). Circles show mean ± SEM. Inset shows resting membrane potential of each cell before (purple) and after (yellow) wash on of CNO. n = 7 cells. ** $p < 0.01$, paired t test.

Figure 6: DREADD inhibition of SST neurons increases decision bias in go/no-go task

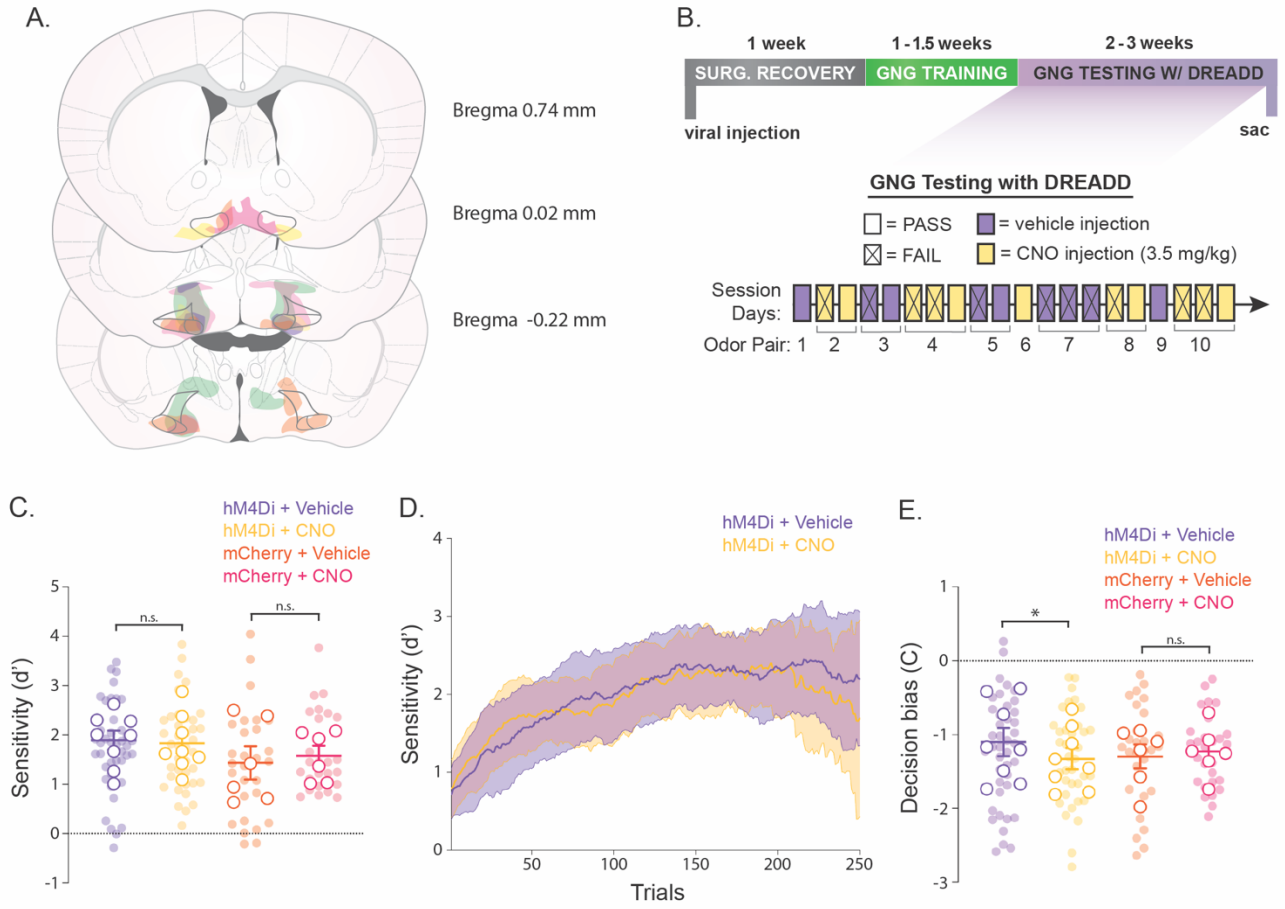

993

994 **Figure 6: DREADD inhibition of SST neurons increases decision bias in the go/no-go task. A.**
995 Quantification of DREADD expression in each animal used for behavioral experiments. Shaded regions
996 represent areas containing cells expressing hM4Di-mCherry across three coronal sections spanning AP
997 from bregma -0.22 – 0.74 mm. Regions are color coded by animal (N = 8). **B.** Timeline of surgery,
998 behavioral training, and behavioral testing with DREADD-mediated inhibition (top) and schematic of the
999 CNO or vehicle injections during testing on different odor pairs (bottom). **C.** Average d' for individual
1000 sessions (transparent circles, n = 30-40) and mouse averages (white circles, N = 6-8) with mean and
1001 SEM of mouse averages. **D.** Performance of mice in the testing phase quantified as a rolling window of
1002 sensitivity (d') across trials. Averages of all CNO-treatment sessions are shown in yellow with 95%
1003 confidence intervals (shaded yellow). Averages of all vehicle-treatment sessions are shown in purple
1004 with 95% confidence intervals (shaded purple). **E.** Average criterion values for individual sessions
1005 (transparent circles) and mouse averages (white circles) with mean and SEM of mouse averages. * $p <$
1006 0.05 paired t test between CNO and vehicle-treated sessions (n = 5 sessions per treatment per mouse)
1007 with hM4Di-expressing animals (N = 8 mice). n.s. $p > 0.05$ paired t test between CNO and vehicle-
1008 treated sessions (n = 5 sessions per treatment per mouse) with mCherry-expressing control animals (N
1009 = 6 mice).